

# Controlling 3-D Morphology of Ni-Fe-Based Nanocatalysts for Oxygen Evolution Reaction

R. H. Manso, Y. Zhu

To be published in "Nanoscale"

February 2019

Condensed Matter Physics and Materials Science Department  
**Brookhaven National Laboratory**

**U.S. Department of Energy**  
USDOE Office of Science (SC), Basic Energy Sciences (BES) (SC-22)

Notice: This manuscript has been authored by employees of Brookhaven Science Associates, LLC under Contract No. DE-SC0012704 with the U.S. Department of Energy. The publisher by accepting the manuscript for publication acknowledges that the United States Government retains a non-exclusive, paid-up, irrevocable, world-wide license to publish or reproduce the published form of this manuscript, or allow others to do so, for United States Government purposes.

## **DISCLAIMER**

This report was prepared as an account of work sponsored by an agency of the United States Government. Neither the United States Government nor any agency thereof, nor any of their employees, nor any of their contractors, subcontractors, or their employees, makes any warranty, express or implied, or assumes any legal liability or responsibility for the accuracy, completeness, or any third party's use or the results of such use of any information, apparatus, product, or process disclosed, or represents that its use would not infringe privately owned rights. Reference herein to any specific commercial product, process, or service by trade name, trademark, manufacturer, or otherwise, does not necessarily constitute or imply its endorsement, recommendation, or favoring by the United States Government or any agency thereof or its contractors or subcontractors. The views and opinions of authors expressed herein do not necessarily state or reflect those of the United States Government or any agency thereof.

1  
2  
3  
4  
5  
6  
7  
8  
9  
10  
11  
12  
13  
14  
15  
16  
17  
18  
19  
20  
21

## Controlling 3-D Morphology of Ni-Fe-Based Nanocatalysts for Oxygen Evolution Reaction

Ryan H. Manso,<sup>1,†</sup> Prashant Acharya,<sup>2,†</sup> Shiqing Deng,<sup>3,4†</sup> Cameron C. Crane,<sup>1</sup> Benjamin Reinhart,<sup>5</sup> Sungsik Lee,<sup>5</sup> Xiao Tong,<sup>6</sup> Dmytro Nykypanchuk,<sup>6</sup> Jing Zhu,<sup>4</sup> Yimei Zhu,<sup>3</sup> Lauren F. Greenlee,<sup>2,\*</sup> and Jingyi Chen<sup>1,\*</sup>

<sup>1</sup>Department of Chemistry and Biochemistry, University of Arkansas, Fayetteville, AR 72701, USA

<sup>2</sup>Ralph E. Martin Department of Chemical Engineering, University of Arkansas, Fayetteville, AR 72701, USA

<sup>3</sup>Condensed Matter Physics and Materials Science Department, Brookhaven National Laboratory, Upton, NY 11973, USA

<sup>4</sup>School of Materials Science and Engineering, Tsinghua University, Beijing 100084, P. R. China

<sup>5</sup>Advanced Photon Source, Argonne National Laboratory, Lemont, IL 60439, USA

<sup>6</sup>Center for Functional Nanomaterials, Brookhaven National Laboratory, Upton, NY 11973, USA

<sup>†</sup>These authors contributed to this work equally.

\*Corresponding authors: chenj@uark.edu (synthesis, characterization) and greenlee@uark.edu (electrocatalysis, characterization)

22 **Abstract:** Controlling the 3-D morphology of nanocatalysts is one of the underexplored but  
23 important approaches for improving the sluggish kinetics of oxygen evolution reaction (OER) in  
24 water electrolysis. This work reports a scalable, oil-based method based on thermal decomposition  
25 of organometallic complexes to yield highly uniform Ni-Fe-based nanocatalysts with well-defined  
26 morphology (i.e., Ni-Fe core-shell, Ni/Fe alloy, and Fe-Ni core-shell). Transmission electron  
27 microscopy reveals their morphology and composition to be NiO<sub>x</sub>-FeO<sub>x</sub>/NiO<sub>x</sub> core-mixed shell,  
28 NiO<sub>x</sub>/FeO<sub>x</sub> alloy, and FeO<sub>x</sub>-NiO<sub>x</sub> core-shell. X-ray techniques resolve the electronic structures of  
29 the bulk and are supported by electron energy loss spectroscopy analysis of individual  
30 nanoparticles. These results suggest the crystal structure of Ni is most likely to contain  $\alpha$ -Ni(OH)<sub>2</sub>  
31 and that the chemical environment of Fe is variable, depending on the morphology of the  
32 nanoparticle. The Ni diffusion from the amorphous Ni-based core to the iron oxide shell makes  
33 the NiO<sub>x</sub>-NiO<sub>x</sub>/FeO<sub>x</sub> core-mixed shell structure the most active and the most stable nanocatalyst,  
34 which outperforms the comparison NiO<sub>x</sub>/FeO<sub>x</sub> alloy nanoparticles expected to be active for OER.  
35 This study suggests that the chemical environment of the mixed NiO<sub>x</sub>/FeO<sub>x</sub> alloy composition is  
36 important to achieve high electrocatalytic activity for OER and that the 3-D morphology plays a  
37 key role in optimization of the electrocatalytic activity and stability of the nanocatalyst for OER.

38  
39  
40

## 41 **Introduction**

42 Water electrolysis can be employed to produce hydrogen and oxygen as an alternative, more  
43 environmentally friendly means to generate clean renewable fuels.<sup>1-2</sup> In principle, water splitting  
44 is straightforward, separating into two half reactions on the cathode (hydrogen evolution reaction,  
45 HER) and anode (oxygen evolution reaction, OER), but the efficiency of the overall reaction  
46 remains limited. One of the major obstacles is the slow kinetics of the four-electron OER, which  
47 requires a much greater applied potential than the thermodynamic standard potential.<sup>1</sup> Finding  
48 catalytic materials to lower the amount of potential applied above the thermodynamic requirement  
49 (i.e., overpotential) remains a necessary task to allow potential viable commercialization of water  
50 electrolysis. Electrocatalysts based on noble metals such as Pt, Ru, Ir, and their oxides have been  
51 extensively investigated for OER due to appreciable activity and relatively high stability.<sup>3-4</sup>  
52 Compared to Pt, Ru, and Ir, their oxides were better catalysts with relatively low overpotentials,  
53 and thus RuO<sub>x</sub> and IrO<sub>x</sub> have been recommended as benchmarks in the development of active  
54 electrocatalysts for OER.<sup>5-7</sup> Despite their superior performance, the high cost of these scarce  
55 materials makes their choice difficult for large-scale industrial use. It is a critical need to search  
56 for inexpensive materials with high catalytic performance for OER to enable practical use in water  
57 electrolyzers.

58 The earth-abundant 3-*d* transition metal-based materials such as Mn, Fe, Co, and Ni oxides  
59 and hydroxides have emerged as promising catalyst candidates for OER under alkaline  
60 conditions.<sup>8-12</sup> Among these low-cost oxides and hydroxides, the Ni-Fe-based materials are among  
61 the most active catalysts, with catalytic activity for OER comparable to that of RuO<sub>x</sub> and IrO<sub>x</sub>.<sup>13-</sup>  
62 <sup>15</sup> Early studies on Ni-based alkaline batteries found that the presence of Fe could lower the OER  
63 overpotential on Ni-based electrodes.<sup>16-17</sup> In the 1980s, Corrigan first reported that the synergistic

64 effects of Fe and Ni on OER activity were the result of a Ni-Fe hydrous oxide composite with  
65 markedly different electrochemical properties compared to either monometallic material alone.<sup>18</sup>  
66 Since then, mixed Ni-Fe-based thin films have been extensively investigated through  
67 electrochemical methods,<sup>19-25</sup> *in situ* spectroscopic tools (e.g., Mössbauer spectroscopy,<sup>26-28</sup>  
68 Raman spectroscopy,<sup>29-31</sup> and x-ray absorption spectroscopy<sup>32-39</sup>) and density functional theory<sup>36,</sup>  
69 <sup>40-42</sup> in an effort to understand reaction mechanisms and elucidate structure-activity relationships.  
70 The early study by Corrigan indicated that coprecipitating as little as 0.01% Fe could significantly  
71 lower the overpotential for OER.<sup>18</sup> Later, it was confirmed by other groups that Fe impurities in  
72 the electrolyte could substantially improve the OER activity of Ni-only materials.<sup>19, 36</sup> The optimal  
73 activity varied with the Fe composition in the films, with some studies showing similar  
74 performance in the range between 10-50%<sup>18, 29</sup> and others indicating 25% to be the optimum.<sup>19-20</sup>  
75 The discrepancy in optimal composition for improved OER activity may be due to the difference  
76 in the preparation methods and the resulting structures of these mixed Ni-Fe-based thin films. The  
77 commonly-used electrodeposition usually generates layered hydroxide structures, while other  
78 synthesis methods can produce different Ni-Fe-based structures. For example, thermal annealing  
79 generated a Fe<sub>3</sub>O<sub>4</sub>-based spinel structure hosted with Ni substitution, forming NiFe<sub>2</sub>O<sub>4</sub>,<sup>34</sup> while an  
80 aerosol-spray-assisted approach produced Ni-Fe-based amorphous materials.<sup>43</sup>

81 Since Ni-Fe-based materials appear to be one of the most active catalysts for OER in these thin  
82 film studies, progress has been recently made to reduce the dimension of these active Ni-Fe-based  
83 materials for improved OER activity. For example, single-layer nanosheets generated by liquid  
84 phase exfoliation of the layered double hydroxides exhibited significantly higher OER activity  
85 than their bulk counterparts.<sup>44</sup> More recent studies by *in situ* electrochemical atomic force  
86 microscopy illustrated the structural dynamics of these nanosheets under electrochemical

87 conditions.<sup>45-46</sup> On the other hand, nanoscale spinel-type Ni-Fe based oxides were synthesized by  
88 a solvothermal method and showed that the  $\text{Ni}_x\text{Fe}_{3-x}\text{O}_4/\text{Ni}$  nanocomposite with an  $x$  value of  $\sim 0.36$   
89 exhibited the most superior activity for OER.<sup>47</sup> While nanocatalysts show promise to improve OER  
90 activity, little effort has been made to explore the morphological effects on the electrocatalytic  
91 performance of Ni-Fe-based nanocatalysts. Our previous multistep aqueous-based synthesis of Ni-  
92 Fe-based nanocatalysts demonstrated that a core-shell morphology having a  $\text{Fe}/\text{Fe}(\text{OH})_3$  core and  
93 a  $\text{Fe}_x\text{Ni}_{1-x}(\text{OH})_2$  shell exhibited a superior OER activity.<sup>48</sup> In this work, we developed a scalable,  
94 oil-based synthesis approach based on thermal decomposition of organometallic complexes that  
95 enables manipulation of both the morphology and crystalline phase of the Ni-Fe nanocatalysts.  
96 Highly uniform Ni-Fe-based nanostructures with different morphologies (i.e., core-shell and alloy)  
97 were synthesized *via* either sequential or simultaneous injection. The uniform nanostructures  
98 enabled us to use transmission electron microscopy (TEM) for in-depth structural and electronic  
99 characterization of a single particle. Together with the x-ray methods on the bulk sample, we  
100 elucidate the morphology, composition, and structure of individual particles for each of these  
101 nanostructures in detail. We then evaluate the OER performance for these well-defined, Ni-Fe-  
102 based nanostructures with Ni and Fe alone nanoparticles. This study allows us to establish a  
103 fundamental understanding of as-synthesized morphological, compositional, and structural  
104 influences on the electrocatalytic activity of Ni-Fe-based nanocatalysts for OER.

## 105 **Results and Discussion**

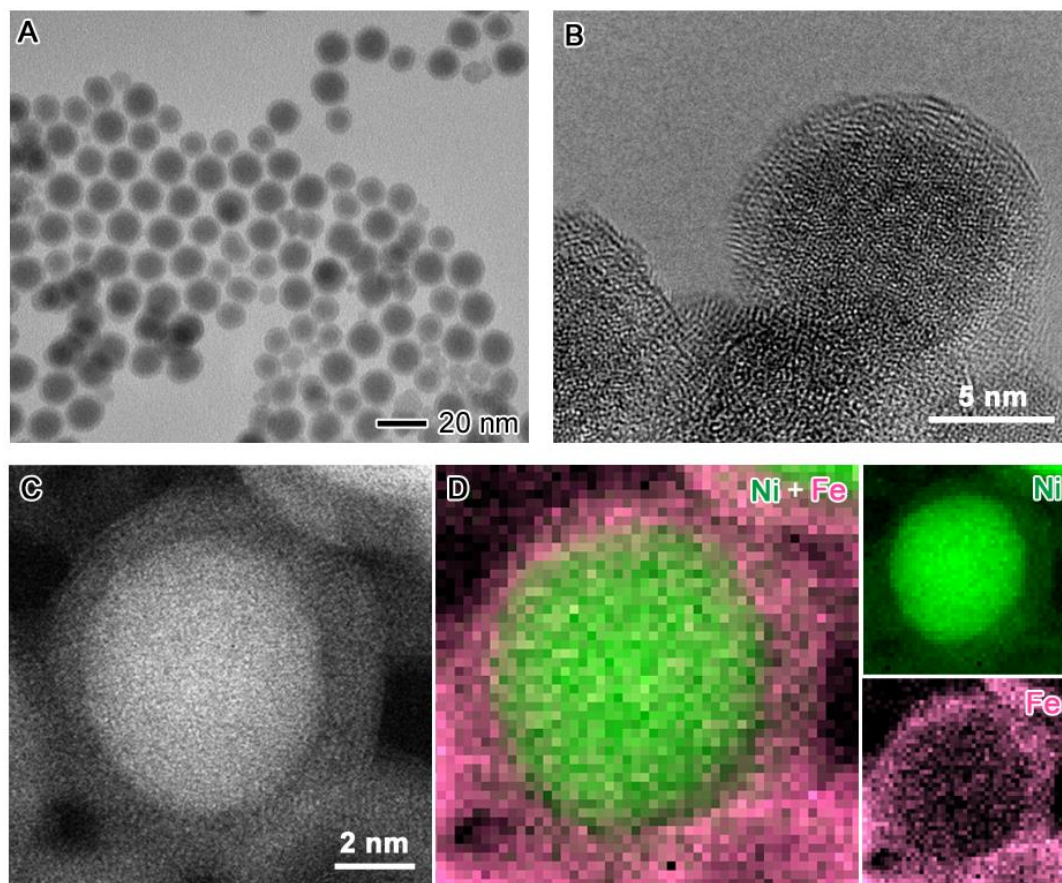
106 Three Ni-Fe-based nanostructures with different morphologies were designed and synthesized  
107 for this study and included Ni-Fe-based core-shell, Ni-Fe-based alloy, and Fe-Ni-based core-shell.  
108 Nanostructure synthesis was achieved through solution-based thermal decomposition of  
109 organometallic complexes in high-boiling-temperature organic solvent. Programmable

110 temperature control was used to improve the uniformity of the resulting nanoparticles. The core-  
111 shell structures were synthesized using a two-step procedure with the first step to synthesize the  
112 cores, followed by the second step to coat the cores with the shells. The alloy structures were  
113 prepared in a one-step synthesis by simultaneously injecting both precursors into the solvent.  
114 During synthesis, the nanoparticles are oxidized when exposed to the ambient atmosphere, and  
115 thus we denote the resulting Ni-Fe-based nanostructures as nickel oxides ( $\text{NiO}_x$ ) and iron oxides  
116 ( $\text{FeO}_x$ ). After synthesis, the nanoparticles were transferred from the organic phase into aqueous  
117 solution through ligand exchange process using polyethylene glycol terminated with carboxylic  
118 acid (PEG-COOH). The overall reaction yield is  $\sim 70\%$  and the estimated cost for the synthesis  
119 was listed in **Table S1**. The analytical TEM, XPS, XRD, and XAS, as well as the electrochemical  
120 characterization were performed on the nanoparticles with PEG-COOH as surface ligands.

121  $\text{NiO}_x$ - $\text{FeO}_x$  core-shell nanoparticles were synthesized by thermally decomposing  $\text{Fe}(\text{CO})_5$   
122 complex in the presence of preformed  $\text{NiO}_x$  seeds. **Figure 1A** displays a representative TEM image  
123 of the reaction product, indicating a core-shell morphology of the nanoparticles. These  
124 nanoparticles are relatively uniform with an overall diameter of  $16.8 \pm 2.0$  nm. The size of the core  
125  $\text{NiO}_x$  nanoparticles is  $12.4 \pm 0.6$  nm (**Figure S1**), and the shell thickness of the core-shell  
126 nanoparticles is estimated to be  $\sim 2.2$  nm. The x-ray photoelectron spectroscopy (XPS) study  
127 indicates that the binding energies of Fe  $2p_{3/2}$  and Ni  $2p_{3/2}$  of the core-shell nanoparticles are at  
128 711.5 eV and  $\sim 856.4$  eV, respectively, confirming the formation of  $\text{FeO}_x$  and  $\text{NiO}_x$  (**Figure S2**).

129 Further characterization of an individual nanoparticle using high-resolution transmission  
130 electron microscopy (HRTEM) and high-angle annular dark-field-scanning transmission electron  
131 microscopy (HAADF-STEM) imaging clearly showed a core-shell morphology, but rather poor  
132 crystallinity (**Figure 1, B and C**). The corresponding electron energy-loss spectroscopy (EELS)

133 mapping of the individual nanoparticle in the HAADF-STEM image reveals elemental distribution  
134 of a Ni-Fe core-shell structure (**Figure 1D**). Quantitative analysis of the EELS mapping reveals  
135 that the overall atomic ratio of Ni to Fe for individual  $\text{NiO}_x\text{-NiO}_x/\text{FeO}_x$  core-mixed shell  
136 nanoparticles is around 1.36 to 1, close to the 1:1 ratio obtained through inductively coupled  
137 plasma mass spectrometry (ICP-MS) of the sample. It is worth noting that Ni is not confined in  
138 the core but diffuses into the shell. The composition of the shell was analyzed by extracting the  
139 signals of Ni and Fe in the ring region, where the shell is projected in the 2-D EELS map (**Figure**  
140 **S3**). The quantitative analysis indicates that a 0.39:1 atomic ratio of Ni:Fe is present in the shell  
141 corresponding to atomic percent of 28% Ni and 72% Fe. Therefore, the  $\text{NiO}_x\text{-FeO}_x$  core-shell  
142 nanoparticles are actually made of a  $\text{NiO}_x$  core and a  $\text{NiO}_x/\text{FeO}_x$  mixed shell, denoted as  $\text{NiO}_x\text{-}$   
143  $\text{NiO}_x/\text{FeO}_x$  core-mixed shell structures.

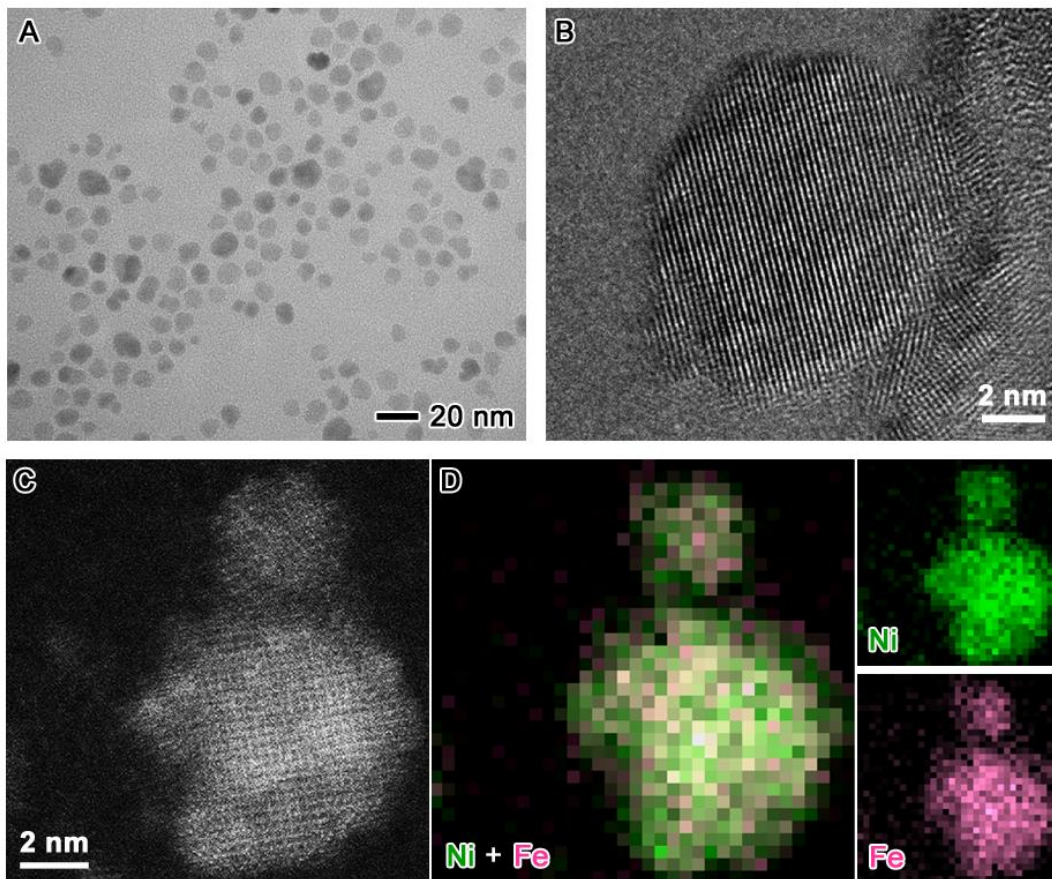


144

145  
146 **Figure 1.** Electron microscopy characterization of NiO<sub>x</sub>-NiO<sub>x</sub>/FeO<sub>x</sub> core-mixed shell  
147 nanoparticles: (A) TEM image overview of the nanoparticles with an average diameter of  $16.8 \pm$   
148  $2.0$  nm; (B,C) HRTEM and HAADF-STEM images displaying a representative nanoparticle in (A)  
149 which is mostly amorphous; (D) EELS mapping of the nanoparticle in (C) with Ni (green), Fe  
150 (pink), and Ni-Fe overlaid maps indicating a NiO<sub>x</sub>-NiO<sub>x</sub>/FeO<sub>x</sub> core-mixed shell morphology. The  
151 Ni/Fe atomic ratio of the shell is 0.39:1.  
152

153 NiO<sub>x</sub>/FeO<sub>x</sub> alloy nanoparticles were prepared using a similar procedure to that of NiO<sub>x</sub>  
154 preparation except that the reactant Ni(acac)<sub>2</sub> alone in the NiO<sub>x</sub> synthesis was replaced by the  
155 mixture of Ni(acac)<sub>2</sub> and Fe(acac)<sub>3</sub> at a 1:1 molar ratio in the alloy nanoparticle synthesis. From  
156 the TEM image in **Figure 2A**, the alloy nanoparticles appear to be more or less spherical in shape  
157 but are less uniform and slightly smaller compared to NiO<sub>x</sub> nanoparticles. The average size of the  
158 alloy nanoparticles is  $9.4 \pm 1.7$  nm. HRTEM image clearly shows the lattice fringes of an alloy  
159 nanoparticle, indicating good crystallinity (**Figure 2B**). No obvious contrast difference is observed  
160 in the HAADF-STEM image, suggesting homogenous distributions of Ni and Fe in a single, or  
161 similar density, phase(s) across the entire nanoparticle (**Figure 2C**). The corresponding EELS  
162 mapping agrees with the observations made from HAADF-STEM image contrast, wherein Ni and  
163 Fe are co-localized evenly across the nanoparticle, indicating an alloy composition (**Figure 2D**).  
164 The XPS spectra of the NiO<sub>x</sub>/FeO<sub>x</sub> nanoparticles in **Figure S2** indicate that the peak position of  
165 the Fe 2p<sub>3/2</sub> and Ni 2p<sub>3/2</sub> binding energies are 712.1 eV and 857.1 eV, respectively, confirming the  
166 oxide formation. The NiO<sub>x</sub>/FeO<sub>x</sub> mixed oxides have higher binding energies than FeO<sub>x</sub> (710.7 eV  
167 for Fe 2p<sub>3/2</sub>) or NiO<sub>x</sub> (856.6 eV for Ni 2p<sub>3/2</sub>). Quantitative analysis of the EELS spectra indicates  
168 that the Ni/Fe atomic ratio of individual particles is  $\sim 0.8$ , which is close to ICP-MS analysis,  
169 showing the overall Ni/Fe atomic ratio of the sample to be 1:1.

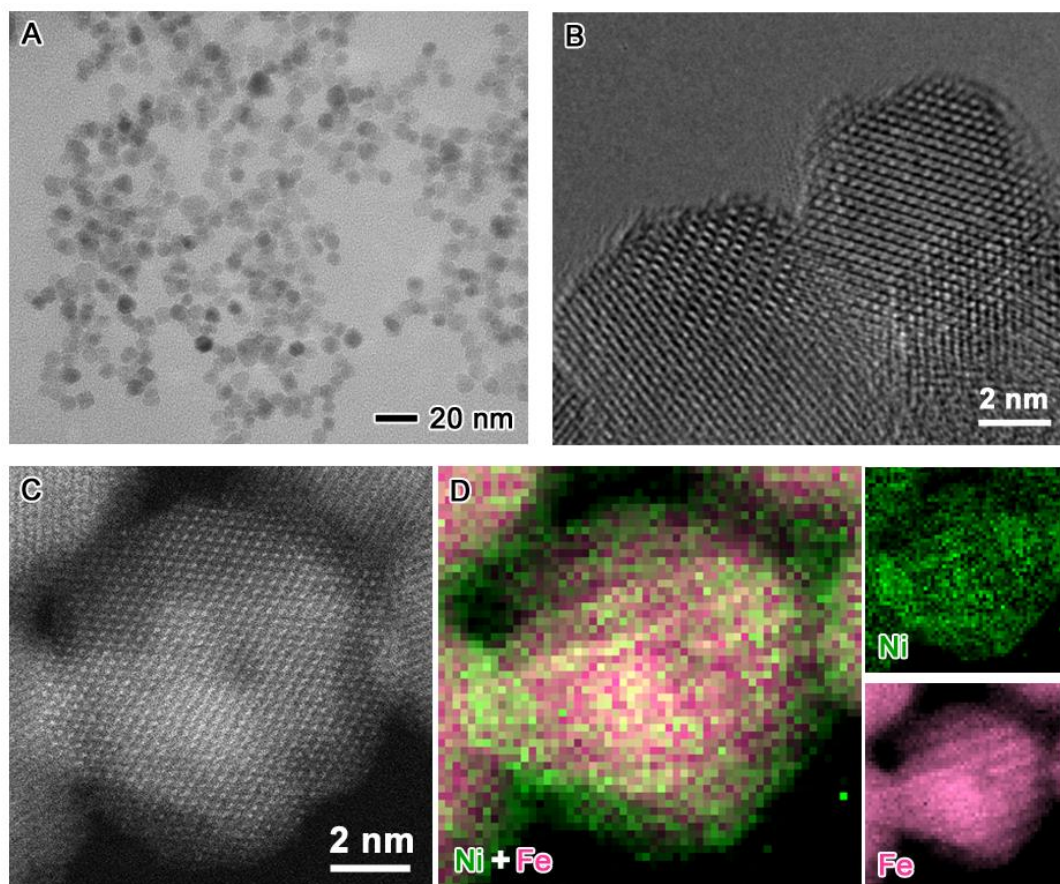
170



171  
 172  
 173 **Figure 2.** Electron microscopy characterization of NiO<sub>x</sub>/FeO<sub>x</sub> alloy nanoparticles: (A) TEM image  
 174 overview of the nanoparticles with an average diameter of  $9.4 \pm 1.7$  nm. (B,C) HRTEM and  
 175 HAADF-STEM images displaying a representative nanoparticle in (A) which is crystalline; (D)  
 176 EELS mapping of the nanoparticle in (C) with Ni (green), Fe (pink), and Ni-Fe overlaid maps  
 177 indicating a NiO<sub>x</sub>/FeO<sub>x</sub> alloy composition.  
 178

179 FeO<sub>x</sub>-NiO<sub>x</sub> core-shell nanoparticles were also synthesized using a two-step procedure by first  
 180 generating the FeO<sub>x</sub> nanoparticles and then coating them with NiO<sub>x</sub> shells. The FeO<sub>x</sub> nanoparticles  
 181 were prepared by thermally decomposing Fe(acac)<sub>3</sub> in a mixture of dibenzyl ether and oleylamine.  
 182 These FeO<sub>x</sub> nanoparticles are spherical in shape with an average diameter of  $9.0 \pm 1.7$  nm  
 183 according to TEM imaging (**Figure S4**). The coating process was performed using thermal  
 184 decomposition of bis(1,5-cyclooctadienenickel(0)) (Ni(COD)<sub>2</sub>) in the presence of the FeO<sub>x</sub>  
 185 nanoparticles. After coating with the Ni shells, the FeO<sub>x</sub>-NiO<sub>x</sub> core-shell nanoparticles have an

186 average diameter of  $9.8 \pm 1.6$  nm, as shown in **Figure 3A**. The shell thickness is estimated to be  
187  $\sim 0.4$  nm. HRTEM result suggests that the nanoparticles exhibit a good crystallinity of the  $\text{FeO}_x$   
188 core, which is covered with an amorphous  $\text{NiO}_x$  shell (**Figure 3B**). In the HAADF-STEM image,  
189 the contrast does not show an obvious core-shell structure (**Figure 3C**); however, the EELS  
190 mapping of an individual nanoparticle indicates that the Ni signal covers a slightly larger area, as  
191 compared to the Fe signal (**Figure 3D**). The Ni/Fe ratio of the entire nanoparticle was calculated  
192 to be around 0.078:1, corresponding to atomic percent 7.2% Ni, which is much less than that  
193 measured from ICP-MS (18.0% Ni). This difference could be attributed to the presence of pure Ni,  
194 possibly from leached Ni or from homogenous, nucleated Ni. The XPS spectra of the  $\text{FeO}_x$ - $\text{NiO}_x$   
195 core-shell nanoparticles in **Figure S3** confirm the oxide composition with the peak positions of  
196 the Fe  $2p_{3/2}$  and Ni  $2p_{3/2}$  binding energies to be 710.7 eV and 855.5 eV, respectively.

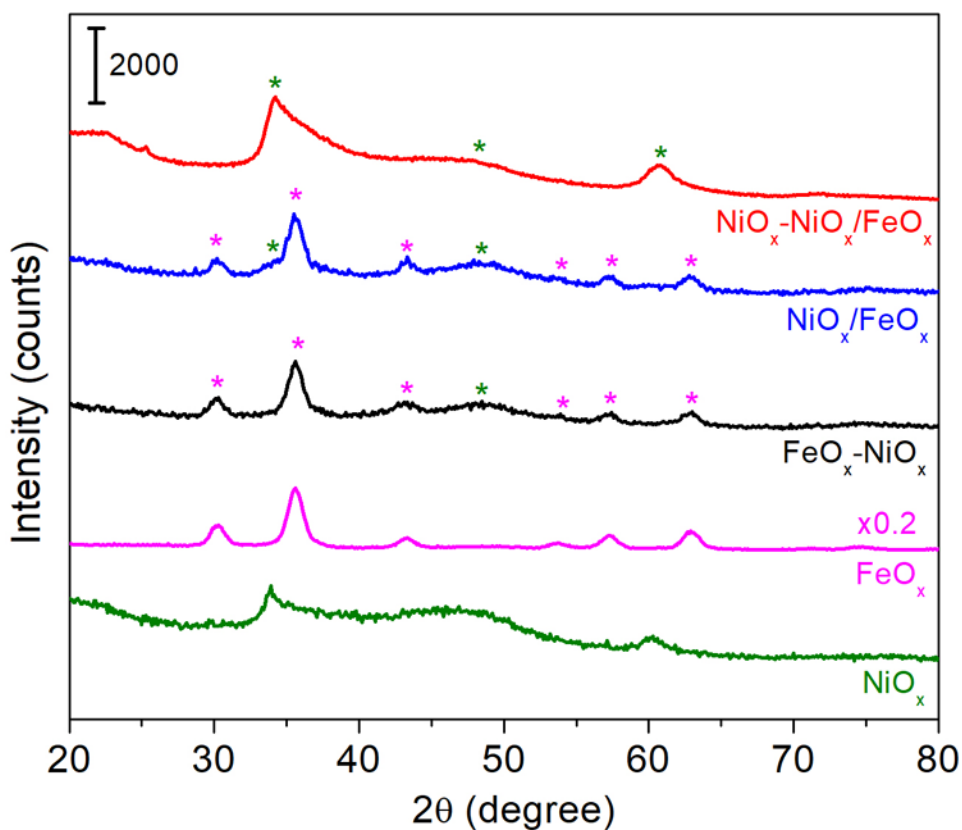


197

198 **Figure 3.** Electron microscopy characterization of FeO<sub>x</sub>-NiO<sub>x</sub> core-shell nanoparticles: (A) TEM  
199 image overview of the nanoparticles with an average diameter of  $9.8 \pm 1.6$  nm; (B,C) HRTEM and  
200 HAADF-STEM images displaying a representative nanoparticle in (A) with a crystalline core and  
201 a thin amorphous shell; (D) EELS mapping of the nanoparticle in (C) with Ni (green), Fe (pink),  
202 and Ni-Fe overlaid maps, confirming the core-shell structure.  
203

204 The crystal structures of these Ni-Fe-based nanoparticles were analyzed by x-ray powder  
205 diffraction (XRD) on the bulk samples, as shown in **Figure 4**. The XRD pattern of the NiO<sub>x</sub>  
206 nanoparticles indicates three broad peaks at 30.4°, 47.0°, and 60.1°, which can be indexed to  $\alpha$ -  
207 Ni(OH)<sub>2</sub> with Ni(II) valence.<sup>49-50</sup> The weak and broad XRD signals are ascribed to the lack of  
208 long-range order in the  $\alpha$ -Ni(OH)<sub>2</sub> crystal structure. According to the XRD pattern, the FeO<sub>x</sub>  
209 nanoparticles could be composed of  $\gamma$ -Fe<sub>2</sub>O<sub>3</sub> with Fe(III) valence and/or Fe<sub>3</sub>O<sub>4</sub> with mixed valence  
210 of Fe(II) and Fe(III). Since Fe(acac)<sub>3</sub> with Fe<sup>3+</sup> was used as the precursor, the FeO<sub>x</sub> nanoparticles  
211 are likely to be  $\gamma$ -Fe<sub>2</sub>O<sub>3</sub>; however, we cannot rule out the possibility of the presence of Fe(II) in  
212 the form of Fe<sub>3</sub>O<sub>4</sub> because the reaction was carried out under a reducing environment with the  
213 presence of oleylamine.<sup>51</sup> The XRD pattern of the NiO<sub>x</sub>-NiO<sub>x</sub>/FeO<sub>x</sub> core-mixed shell nanoparticles  
214 is essentially the same as that of NiO<sub>x</sub> with three broad peaks at 30.4°, 47.0°, and 60.1°, suggesting  
215 that the mixed NiO<sub>x</sub>/FeO<sub>x</sub> shell is largely amorphous consistent with HRTEM result in Figure 1B.  
216 According to our previous study, the thermal decomposition of Fe(CO)<sub>5</sub> at the early stage when  
217 reaction temperature was relatively low (180 °C) yielded mostly amorphous FeO<sub>x</sub>; if any  
218 crystallinity is present, it should be below the detection limit of XRD (< 2%).<sup>52</sup> Based on these  
219 results, it is suggested that the core-shell nanoparticles are made of  $\alpha$ -Ni(OH)<sub>2</sub> and Fe<sub>3</sub>O<sub>4</sub>. For the  
220 NiO<sub>x</sub>/FeO<sub>x</sub> alloy nanoparticles, the XRD pattern appears to be a mixture of  $\alpha$ -Ni(OH)<sub>2</sub> and iron  
221 oxide(s). Similar to the FeO<sub>x</sub> nanoparticles, the FeO<sub>x</sub> in the alloy is likely to be  $\gamma$ -Fe<sub>2</sub>O<sub>3</sub> due to the  
222 same precursor Fe(acac)<sub>3</sub> used in the synthesis. Compared to that of the FeO<sub>x</sub> nanoparticles, the  
223 XRD pattern of FeO<sub>x</sub>-NiO<sub>x</sub> core-shell nanoparticles exhibits an additional broad peak at 47.0° that

224 can be assigned to  $\alpha$ -Ni(OH)<sub>2</sub>. The weak  $\alpha$ -Ni(OH)<sub>2</sub> is due to a small amount (~10 atomic%) of Ni  
 225 in the FeO<sub>x</sub>-NiO<sub>x</sub> core-shell nanoparticles. The presence of  $\alpha$ -Ni(OH)<sub>2</sub> as the primary phase for  
 226 Ni atoms is promising for the OER because this more disordered phase of nickel hydroxide is now  
 227 known to be the more active phase for alkaline OER.<sup>19</sup> The presence of peaks for iron oxide phases  
 228 does suggest that at least some, or perhaps all, of the Fe atoms are present in a separate oxide phase  
 229 in the as-synthesized nanoparticles. However, it is also possible that some of the Fe and Ni atoms  
 230 are present in a combined hydroxide phase, as has been suggested for other Fe-Ni hydroxide/oxide  
 231 materials.<sup>22, 36</sup>

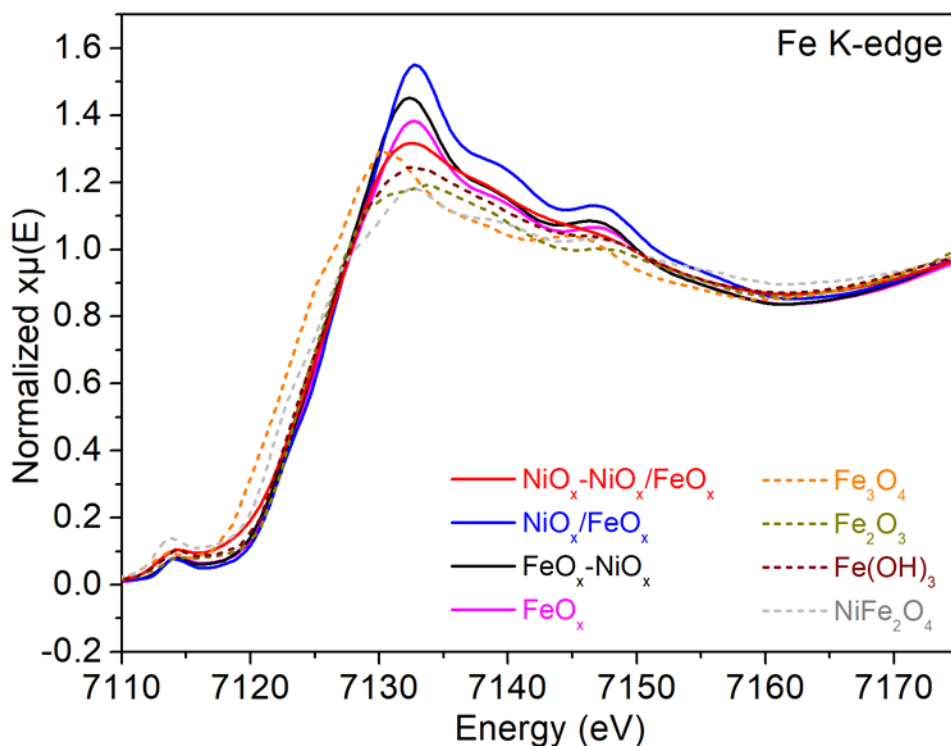


232  
 233  
 234 **Figure 4.** XRD patterns of different nanoparticle samples: NiO<sub>x</sub>-NiO<sub>x</sub>/FeO<sub>x</sub> core-mixed shell (red),  
 235 NiO<sub>x</sub>/FeO<sub>x</sub> alloy (blue), FeO<sub>x</sub>-NiO<sub>x</sub> core-shell (black), FeO<sub>x</sub> (pink), and NiO<sub>x</sub> (green). The peaks  
 236 assigned to  $\alpha$ -Ni(OH)<sub>2</sub> are labelled by green stars while the peaks indexed to Fe<sub>3</sub>O<sub>4</sub> or  $\gamma$ -Fe<sub>2</sub>O<sub>3</sub> are  
 237 labelled by pink stars.  
 238

239 *Ex situ* XAS was performed on this series of nanocatalysts to examine the collective  
240 composition and structure of each nanocatalyst. The spectra for Fe are plotted in **Figure 5**,  
241 supplemented with a full set of Fe standard spectra plotted in **Figure S5**. The spectral shapes of  
242 the Fe K-edge for FeO<sub>x</sub> nanoparticles, FeO<sub>x</sub>-NiO<sub>x</sub> core-shell nanoparticles, and the NiO<sub>x</sub>/FeO<sub>x</sub>  
243 alloy nanoparticles appear quite similar. However, at the white line, the peak intensity is noticeably  
244 different for the three samples, and the peak position of the edge is shifted slightly to higher eV  
245 for FeO<sub>x</sub> and NiO<sub>x</sub>/FeO<sub>x</sub>. When comparing across different sample morphologies and metal  
246 compositions, an increase in peak height can suggest an increase in order or crystallinity, while a  
247 shift to higher eV most likely suggests a larger portion of the Fe atoms are in a higher oxidation  
248 state. These results support HRTEM and XRD results, where NiO<sub>x</sub>/FeO<sub>x</sub> and FeO<sub>x</sub>-NiO<sub>x</sub>  
249 nanoparticles were both found to be more crystalline than the NiO<sub>x</sub>-NiO<sub>x</sub>/FeO<sub>x</sub> core-mixed shell  
250 nanoparticle sample. The shift to slightly higher eV for FeO<sub>x</sub> suggests that more of the Fe atoms  
251 are likely to be in the 3+ oxidation state, rather than in the 2+ oxidation state, a conclusion that is  
252 also supported by the discussion above and the use of a Fe<sup>3+</sup> precursor during synthesis. Similarly,  
253 the NiO<sub>x</sub>/FeO<sub>x</sub> alloy nanoparticle sample, also synthesized from the Fe<sup>3+</sup> precursor, has an edge  
254 position that is shifted slightly to higher eV, as compared to the FeO<sub>x</sub>-NiO<sub>x</sub> core-shell nanoparticle  
255 sample. This result could be explained by the synthesis process in which the FeO<sub>x</sub> nanoparticles  
256 from the same synthesis were used as seeds for core-shell nanoparticle growth. Even though the  
257 FeO<sub>x</sub>-NiO<sub>x</sub> core-shell nanoparticles were synthesized starting with the FeO<sub>x</sub> nanoparticles, which  
258 would suggest that that Fe K-edge position should also be shifted to higher eV and match that of  
259 the NiO<sub>x</sub>/FeO<sub>x</sub> and FeO<sub>x</sub> samples, the edge is in fact positioned at a slightly lower eV. This result  
260 is consistent with the EELS Fe L<sub>2,3</sub>-edge results in **Figure 7** and suggests that the Fe atoms were  
261 in a more electron-rich chemical environment in this sample. The pre-edge features of all three

262 samples are quite similar in shape and position and align most closely with the  $\text{NiFe}_2\text{O}_4$  pre-edge  
263 position, albeit with a lower pre-edge intensity. The lower pre-edge intensity suggests an  
264 octahedral coordination environment, and the lower pre-edge intensity combined with the lower  
265 eV edge position suggest an iron phase that has Fe(II) and Fe(III) species. While the edge is not  
266 shifted fully to the lower eV position of the  $\text{Fe}_3\text{O}_4$  reference material, the slight shift is suggestive  
267 of some of the Fe atoms having a lower oxidation state, similar to that of a  $\text{Fe}_3\text{O}_4$ -like phase,  
268 perhaps in combination with a  $\text{Fe}_2\text{O}_3$ -like phase. The minor shift suggests a small contribution of  
269 more electron-rich Fe atoms to the overall ensemble of Fe in the nanoparticles.

270 For the  $\text{NiO}_x\text{-NiO}_x/\text{FeO}_x$  core-mixed shell nanoparticle sample, the Fe K-edge spectrum  
271 exhibited features that are quite different from that of  $\text{NiO}_x/\text{FeO}_x$  alloy or  $\text{FeO}_x\text{-NiO}_x$  core-shell  
272 nanoparticles. This result may potentially be in part because the  $\text{Fe}(\text{CO})_5$  precursor was used in  
273 place of  $\text{Fe}(\text{acac})_3$ . However, the result may also be a result of the different core-shell morphology  
274 that was formed and the presence of Fe in the iron oxide shell. The edge peak is broad and has a  
275 decreased intensity, as compared to the other samples. This result suggests a more disordered  
276 structure to the nanoparticles, as well as a population of oxidation states within the nanoparticle.  
277 By comparing with spectra of the standard samples, the Fe in this sample is likely to be a mixture  
278 of 2+/3+ state, which also agrees with the XRD results. The slightly higher intensity pre-edge  
279 suggests a distorted octahedral structure. This change in the pre-edge feature may be a result of  
280 the mixed metal oxide/hydroxide shell, where the presence of both metals in an oxide/hydroxide  
281 phase would likely cause distortions in the coordination chemistry of the Fe.



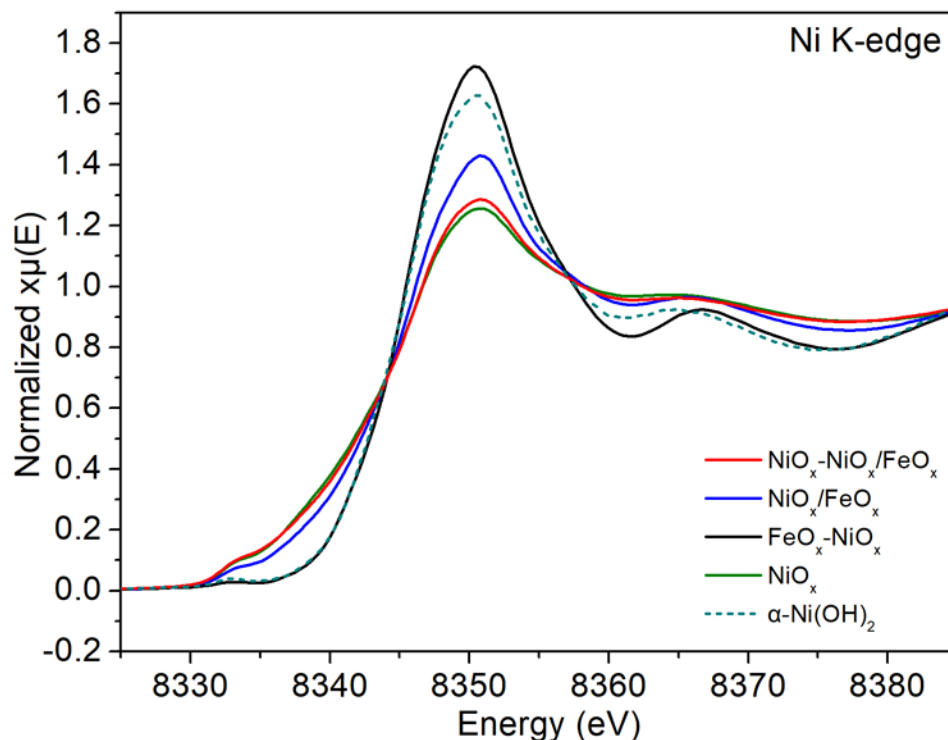
282  
 283  
 284 **Figure 5.** XAS spectra of Fe K-edge for the nanoparticle catalysts: NiO<sub>x</sub>-NiO<sub>x</sub>/FeO<sub>x</sub> core-mixed  
 285 shell (red), NiO<sub>x</sub>/FeO<sub>x</sub> alloy (blue), FeO<sub>x</sub>-NiO<sub>x</sub> core-shell (black), and FeO<sub>x</sub> (pink). The XAS  
 286 spectra of selected Fe bulk standards were plotted in dash curves: Fe<sub>3</sub>O<sub>4</sub> (orange), Fe<sub>2</sub>O<sub>3</sub> (dark  
 287 yellow), Fe(OH)<sub>3</sub> (wine), and NiFe<sub>2</sub>O<sub>4</sub> (grey).  
 288

289 The EXAFS region (**Figure S6**) suggests slight differences in Fe-O bond length in the first  
 290 coordination sphere amongst the experimental samples, along with a shoulder around 1 Å, which  
 291 is indicative of a contribution from iron hydroxide and similar to EXAFS spectra obtained for the  
 292 Fe K edge of other Fe<sub>x</sub>Ni<sub>y</sub>(OH)<sub>z</sub> materials.<sup>36, 53</sup> All experimental samples appear to have an Fe-O  
 293 bond length that is slightly larger than the most relevant reference material, Fe<sub>3</sub>O<sub>4</sub>, and the NiO<sub>x</sub>-  
 294 NiO<sub>x</sub>/FeO<sub>x</sub> core-mixed shell nanoparticle sample resulted in a slightly larger bond length than the  
 295 other experimental samples. The second coordination sphere metal-metal distances (Fe-O-Fe/Ni)  
 296 also vary as a function of the different experimental samples and as compared to the reference  
 297 materials. Generally, there appears to be more variability in the second coordination sphere than  
 298 in the first coordination sphere, which may result from the influences of Fe-Ni substitution and

309 phase structural differences as a result of the different morphologies synthesized in nanoparticle  
300 form. The broad peak obtained for core-shell FeO<sub>x</sub>-NiO<sub>x</sub> is suggestive of the Fe<sub>3</sub>O<sub>4</sub> reference  
301 material spectra,<sup>54-56</sup> with less well-defined peak separation within the second coordination sphere;  
302 this peak splitting is caused by the multiple chemical environments of the Fe atoms, and thus  
303 multiple Fe-O-Fe metal-metal distances, in the Fe<sub>3</sub>O<sub>4</sub> crystal structure, nominally described as an  
304 Fe(II)/Fe(III) mixed oxidation state material. The peak of the second coordination sphere for FeO<sub>x</sub>  
305 vs NiO<sub>x</sub>/FeO<sub>x</sub> is less broad and is positioned at shorter vs longer radial distance, respectively. The  
306 peak of the second coordination sphere for the core-mixed shell NiO<sub>x</sub>-NiO<sub>x</sub>/FeO<sub>x</sub> has significantly  
307 lower peak intensity, suggesting structural disorder. The peak is also more narrow than those of  
308 the other experimental samples and is located at lower radial distance, as compared to NiO<sub>x</sub>/FeO<sub>x</sub>;  
309 lower radial distance is suggestive of a compressed Fe-O-M metal-metal bond distance.

310 The spectra for Ni are plotted in **Figure 6**, supplemented with a full set of Ni standard spectra  
311 plotted in **Figure S7**. The spectral shapes of the Ni K-edge for the NiO<sub>x</sub>-NiO<sub>x</sub>/FeO<sub>x</sub> core-mixed  
312 shell nanoparticles and the NiO<sub>x</sub> nanoparticles had nearly identical features in both the pre-edge  
313 and the white line edge. This result clearly indicates that the majority of the Ni atoms in the NiO<sub>x</sub>-  
314 NiO<sub>x</sub>/FeO<sub>x</sub> core-mixed shell nanoparticles were in a chemical environment like that of the NiO<sub>x</sub>  
315 nanoparticles, which is likely to be α-Ni(OH)<sub>2</sub>, based on the XRD results. The NiO<sub>x</sub>/FeO<sub>x</sub> alloy  
316 nanoparticles resulted in a pre-edge shape and intensity that was quite similar to the NiO<sub>x</sub> and  
317 NiO<sub>x</sub>-NiO<sub>x</sub>/FeO<sub>x</sub> nanoparticles. All three samples have a pre-edge intensity that is higher than that  
318 of the α-Ni(OH)<sub>2</sub> reference material, suggesting that the Ni species of these three samples are in a  
319 distorted octahedral coordination geometry, rather than the octahedral geometry expected for α-  
320 Ni(OH)<sub>2</sub>. In contrast, the pre-edge of the FeO<sub>x</sub>-NiO<sub>x</sub> core-shell nanoparticles matches the shape  
321 and intensity of α-Ni(OH)<sub>2</sub>, suggesting the Ni atoms are in an octahedral coordination environment

322 typical of the alpha hydroxide phase. This conclusion is further supported by the similar white line  
323 edge position and peak intensity of the FeO<sub>x</sub>-NiO<sub>x</sub> core-shell nanoparticles, as compared to the α-  
324 Ni(OH)<sub>2</sub> reference material. Across the set of experimental samples, all of the samples displayed  
325 an edge position indicative of α-Ni(OH)<sub>2</sub>, and thus, the Ni was likely in 2+ state.<sup>22</sup>



326

327 **Figure 6.** XAS spectra of Ni K-edge for the nanoparticle catalysts: NiO<sub>x</sub>-NiO<sub>x</sub>/FeO<sub>x</sub> core-mixed  
328 shell (red), NiO<sub>x</sub>/FeO<sub>x</sub> alloy (blue), FeO<sub>x</sub>-NiO<sub>x</sub> core-shell (black), and NiO<sub>x</sub> (green). The XAS  
329 spectrum of α-Ni(OH)<sub>2</sub> bulk standard was plotted in a dark green dash curve.

330

331 Similar to the results for the Fe K edge, the EXAFS region (**Figure S8**) suggests slight shifts  
332 in Ni-O first coordination sphere bond distances. However, the variability observed in the Fe  
333 EXAFS region for the second coordination sphere is not apparent in the Ni EXAFS region for the  
334 Ni second coordination sphere (Ni-O-Ni/Fe). This result may suggest that some of the differences  
335 observed in nanoparticle structure and, ultimately, electrochemical performance, are a result of  
336 differences in the chemical coordination environment of the Fe, more so than the Ni, species in

337 these nanoparticle materials. The shape and peak position of the second coordination sphere is  
338 quite similar to that of the  $\alpha$ -Ni(OH)<sub>2</sub> reference material for all of the experimental samples.

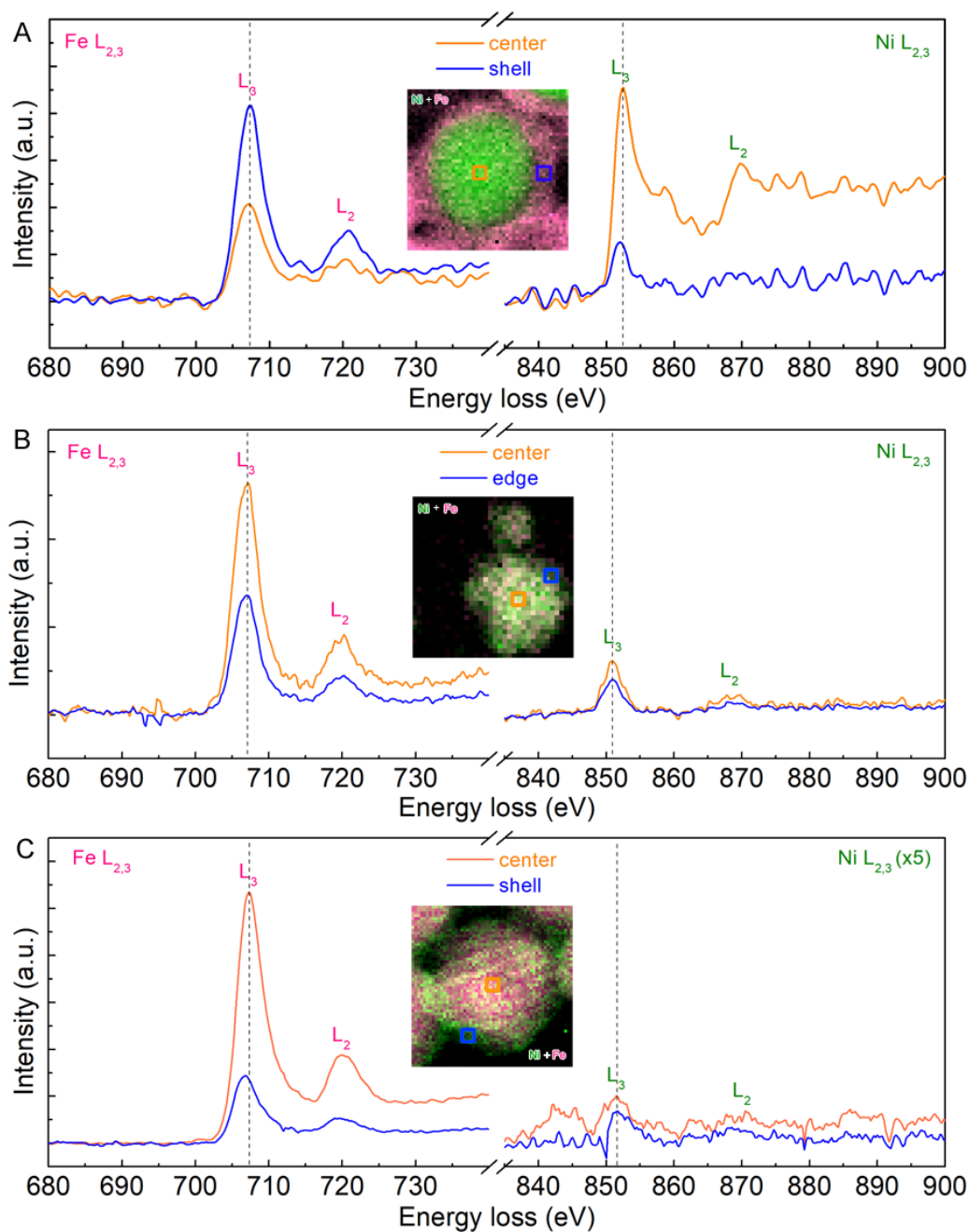
339 Further analysis of EELS data from individual nanoparticles reveals the differences in local  
340 chemical states of Fe and Ni between the core and the shell in the core-shell structures and provides  
341 results that correspond well with XAS data on the bulk samples. **Figure 7** displays the EELS  
342 spectra of the Ni and Fe L<sub>2,3</sub>-edges extracted from the center and the edge of the core-shell  
343 nanoparticles (i.e., NiO<sub>x</sub>-NiO<sub>x</sub>/FeO<sub>x</sub> core-mixed shell and FeO<sub>x</sub>-NiO<sub>x</sub> core-shell) and the  
344 NiO<sub>x</sub>/FeO<sub>x</sub> alloy nanoparticle. No peak shifts for both the Fe and Ni L<sub>2,3</sub>-edges were found for the  
345 alloy nanoparticles, suggesting the uniform chemical environment of both Fe and Ni across the  
346 nanoparticle, but shifts of the peak positions were observed in the EELS spectra for the core-shell  
347 structures. Based on the shift of the energy onset, the relative oxidation state,<sup>57-58</sup> coordination  
348 environment,<sup>58-60</sup> and electron density of elements in the center and the shell can be compared. The  
349 lower energy onset can correspond to a lower oxidation state or an electron rich state of the element  
350 due to the screening effect of outer-shell electrons.<sup>61-62</sup> For iron, a shift to lower energy onset may  
351 also suggest a shift in coordination from octahedral to tetrahedral. The direct comparison of the  
352 core and shell energy onset, however, is not straightforward because TEM is a 2-D projection of  
353 an object and thus each center spectrum contains the information of both the core and shell.  
354 Nonetheless, comparing the center and shell spectra, the energy shifts could provide evidence for  
355 local chemical environment changes of elements.

356 For NiO<sub>x</sub>-NiO<sub>x</sub>/FeO<sub>x</sub> core-mixed shell nanoparticles, the energy positions of the Fe L<sub>2,3</sub>-edges  
357 in the center and shell spectra are essentially the same because there is no Fe in the core and both  
358 spectra indicate the Fe in the shell. For Ni, however, the energy onset of the L<sub>3</sub> edge in the shell is  
359 0.5 eV lower than that in the center. Although the center spectrum contains the Ni signal from

360 both the core and the shell, most of the Ni signal is contributed from the pure Ni core because the  
361 shell is very thin, with a thickness that is 1/8<sup>th</sup> of the core diameter, and is composed of a mixture  
362 of Ni and Fe at an atomic ratio of 0.39/1. Prior work has shown that a shift to lower eV can be due  
363 to the presence of nickel metal rather than nickel oxide.<sup>58</sup> However, research has also shown that  
364 when metal atoms are incorporated into a nanostructured material, L<sub>2,3</sub> edge shifts may also occur  
365 and are thought, generally, to result from shifts in bi-metallic influences on coordination<sup>60</sup> and spin  
366 state.<sup>63</sup> It is unlikely that the Ni atoms in the shell of these nanoparticles experienced a full  
367 oxidation state change from Ni<sup>2+</sup> to Ni<sup>0</sup>; however, the Fe atoms present in the shell can contribute  
368 electron density to the Ni atoms. Thus, we might interpret the onset energy shift of the Ni in the  
369 shell as likely due to the contributions of electron transfer from surrounding Fe in the shell, which  
370 provide electron-rich Ni on the surface of the NiO<sub>x</sub>-NiO<sub>x</sub>/FeO<sub>x</sub> core-mixed shell nanoparticles.  
371 This shift could also be a result of the strain effects; however, further analysis of the crystal  
372 structure difference at the core-shell interface is needed in order to determine the strain states.<sup>64</sup>  
373 Additional evidence for the proposed electron transfer or electron donation from Fe to Ni is  
374 supported by the Fe K edge EXAFS, where the smaller radial distance of the second coordination  
375 sphere suggests a compressed Fe-O-M bond distance and loss of electron density, along with the  
376 XPS results as shown in **Figure S2**. The binding energy of Fe 2p electrons for NiO<sub>x</sub>-NiO<sub>x</sub>/FeO<sub>x</sub>  
377 increased by 0.8 eV compared to that for FeO<sub>x</sub> while the binding energy of Ni 2p electrons for  
378 NiO<sub>x</sub>-NiO<sub>x</sub>/FeO<sub>x</sub> decreased by 0.2 eV compared to that for NiO<sub>x</sub>. These corroborative results  
379 suggest that electrons are preferentially transferred or donated from Fe to Ni in the shell of the  
380 NiO<sub>x</sub>-NiO<sub>x</sub>/FeO<sub>x</sub> core-mixed shell nanostructures.

381 In contrast, for the FeO<sub>x</sub>-NiO<sub>x</sub> core-shell nanoparticles, no difference was observed in the peak  
382 position of the Ni L<sub>3</sub>-edge in EELS spectra while a 0.5 eV shift to lower energy for the peak

383 position of the Fe L<sub>3</sub>-edge was observed in the shell spectrum compared to the center spectrum.  
384 The shift to lower energy suggests the presence of Fe(II) species, which is supported by our  
385 previous analysis of the Fe K-edge spectra. This energy onset decrease in eV for the Fe at the  
386 interface of the core-shell nanoparticles could be attributed to the deposition of metallic Ni from  
387 the thermal decomposition of the Ni(0) organometallic complex thermal deposition, leading to an  
388 electron-rich environment for the surface Fe. The XPS data also indicates that Ni is more electron-  
389 rich in FeO<sub>x</sub>-NiO<sub>x</sub> core-shell nanoparticles than in NiO<sub>x</sub> nanoparticles, which is likely due to the  
390 use of precursors with different valence (Ni<sup>0</sup> versus Ni<sup>2+</sup>) in the corresponding synthesis. This  
391 result is consistent with XAS results that the Fe K edge of FeO<sub>x</sub>-NiO<sub>x</sub> core-shell is in fact  
392 positioned at a lower eV compared to FeO<sub>x</sub>.



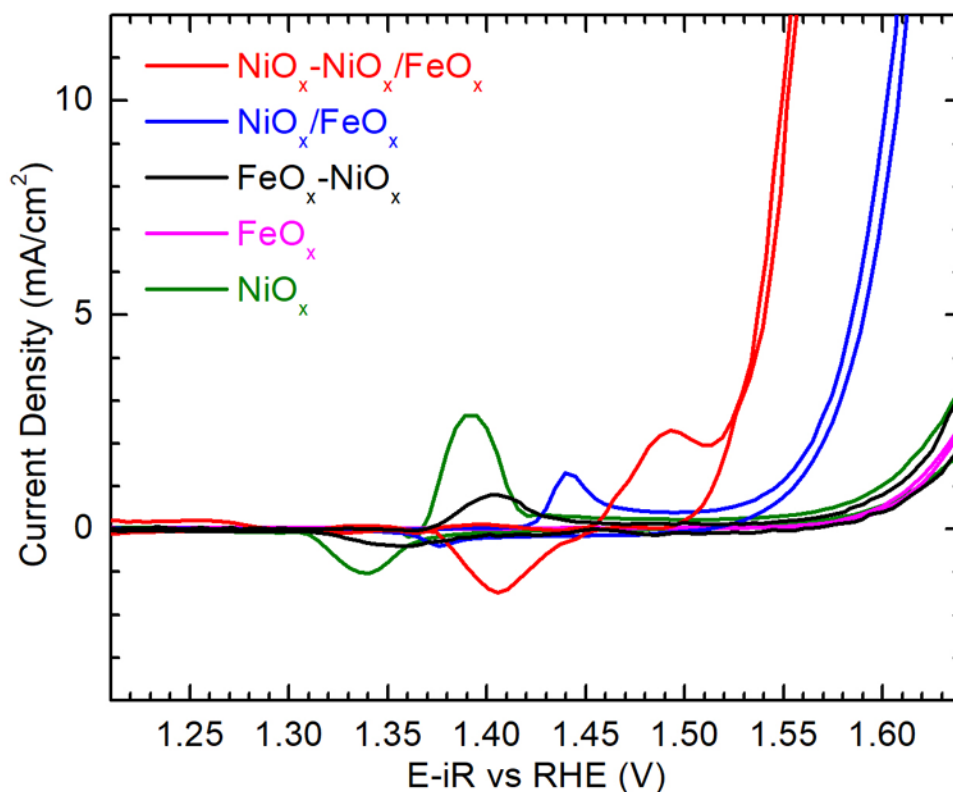
393

394 **Figure 7.** EELS spectra of Ni and Fe  $L_{2,3}$ -edges extracted from the center region (orange box) and  
 395 the shell region (blue box) of each nanoparticle displayed in the inset of each panel: (A)  $\text{NiO}_x$ -  
 396  $\text{NiO}_x/\text{FeO}_x$  core-mixed shell nanoparticle showing that the energy positions of the Fe  $L_{2,3}$ -edges in  
 397 the center and shell spectra were essentially the same while the energy onset of the Ni  $L_3$  edge in  
 398 the shell was 0.5 eV lower than that in the center. (B)  $\text{NiO}_x/\text{FeO}_x$  alloy nanoparticle indicating no  
 399 peak shifts for both the Fe and Ni  $L_{2,3}$ -edges. (C)  $\text{FeO}_x$ - $\text{NiO}_x$  core-shell nanoparticle showing that  
 400 no difference was observed in the peak position of the Ni  $L_3$ -edge while a 0.5 eV shift to lower  
 401 energy for the peak position of the Fe  $L_3$ -edge was observed in the shell spectrum compared to the  
 402 center spectrum.

403

404 The three different morphologies of Ni-Fe-based nanostructures (i.e., NiO<sub>x</sub>-NiO<sub>x</sub>/FeO<sub>x</sub> core-  
405 mixed shell, NiO<sub>x</sub>-FeO<sub>x</sub> alloy, and FeO<sub>x</sub>-NiO<sub>x</sub> core-shell) along with the controls (i.e., NiO<sub>x</sub> and  
406 FeO<sub>x</sub>) were evaluated for OER. The OER activity of the nanoparticles was assessed by their cyclic  
407 voltammetry (CV) profile in 1 M KOH. **Figure 8** shows the CV profile comparison of these  
408 nanocatalysts. The NiO<sub>x</sub>-NiO<sub>x</sub>/FeO<sub>x</sub> core-mixed shell nanoparticles exhibited the best  
409 performance with the lowest onset potential, which reached the benchmark current density of 10  
410 mA/cm<sup>2</sup> at 1.55 V vs RHE. Switching another water-soluble surface ligand such as PEG-NH<sub>2</sub>  
411 increased the onset potential by 60 mV (**Figure S9**). The NiO<sub>x</sub>-FeO<sub>x</sub> alloy nanoparticles had the  
412 second lowest onset potential and reached 10 mA/cm<sup>2</sup> at 1.60 V vs RHE. The remaining  
413 nanocatalysts were rather poor OER electrocatalysts, showing much higher onset potentials. The  
414 two bimetallic nanocatalysts (i.e., NiO<sub>x</sub>-NiO<sub>x</sub>/FeO<sub>x</sub> core-mixed shell and NiO<sub>x</sub>/FeO<sub>x</sub> alloy)  
415 drastically outperformed the two monometallic nanocatalysts (i.e. NiO<sub>x</sub> or FeO<sub>x</sub> alone), which  
416 agrees with the literature reported on the thin film studies.<sup>19, 22, 36, 65</sup> Another bimetallic  
417 nanocatalyst (FeO<sub>x</sub>-NiO<sub>x</sub> core-shell) did not improve the onset potential compared to NiO<sub>x</sub> or FeO<sub>x</sub>,  
418 suggesting that the 3-D morphology has a significant influence on the electrocatalytic activity of  
419 the NiFe-based nanocatalysts. This result is also likely driven by the composition of the iron and  
420 nickel at the surface of the nanoparticles, where the atomic composition of Ni in the FeO<sub>x</sub>-NiO<sub>x</sub>  
421 core-shell nanoparticles was quite low (7.2%). We expect, based on prior literature,<sup>19, 22, 29, 36, 65-66</sup>  
422 that an Fe/Ni atomic ratio in the range of 20-80 to 50-50 will be the most active for OER.  
423 Interestingly, the NiO<sub>x</sub>/FeO<sub>x</sub> alloy nanoparticles fit this parameter range, but the NiO<sub>x</sub>-NiO<sub>x</sub>/FeO<sub>x</sub>  
424 core-mixed shell nanoparticles do not fit this expectation, based on our compositional analysis  
425 from EELS. We thus attribute the OER activity of the NiO<sub>x</sub>-NiO<sub>x</sub>/FeO<sub>x</sub> nanoparticles to the  
426 modified electronic structure of the Fe and Ni atoms in the mixed metal shell, where it appears

427 from EELS and XPS analysis that the Ni atoms are more electron rich, while the Fe atoms likely  
428 are donating electrons to the Ni atoms.



429  
430  
431 **Figure 8.** CV profiles of the nanoparticle catalysts obtained in 1 M KOH at a scan rate of 10 mV/s:  
432 NiO<sub>x</sub>-NiO<sub>x</sub>/FeO<sub>x</sub> core-mixed shell (red), NiO<sub>x</sub>/FeO<sub>x</sub> alloy (blue), FeO<sub>x</sub>-NiO<sub>x</sub> core-shell (black),  
433 FeO<sub>x</sub> (pink), and NiO<sub>x</sub> (green).

434  
435 The difference in 3-D morphology of these nanocatalysts also impacts the characteristic Ni  
436 redox peak in the region of 1.30 – 1.53 V of CV profiles. The NiO<sub>x</sub> nanoparticles exhibited the  
437 largest area for the Ni redox peaks, which occurred at the lowest potential among all the  
438 nanocatalysts. As can be seen from the CV data, the height of the Ni redox peak does not  
439 necessarily correlate directly with OER activity; NiO<sub>x</sub> alone is expected to have a distinct redox  
440 peak but low OER activity in purified alkaline electrolyte, as there are no Fe atoms present to  
441 enhance the OER reaction. The FeO<sub>x</sub>-NiO<sub>x</sub> core-shell nanocatalyst has a small characteristic Ni  
442 redox peak despite the presence of Ni; this small peak is likely an indication of the low Ni content

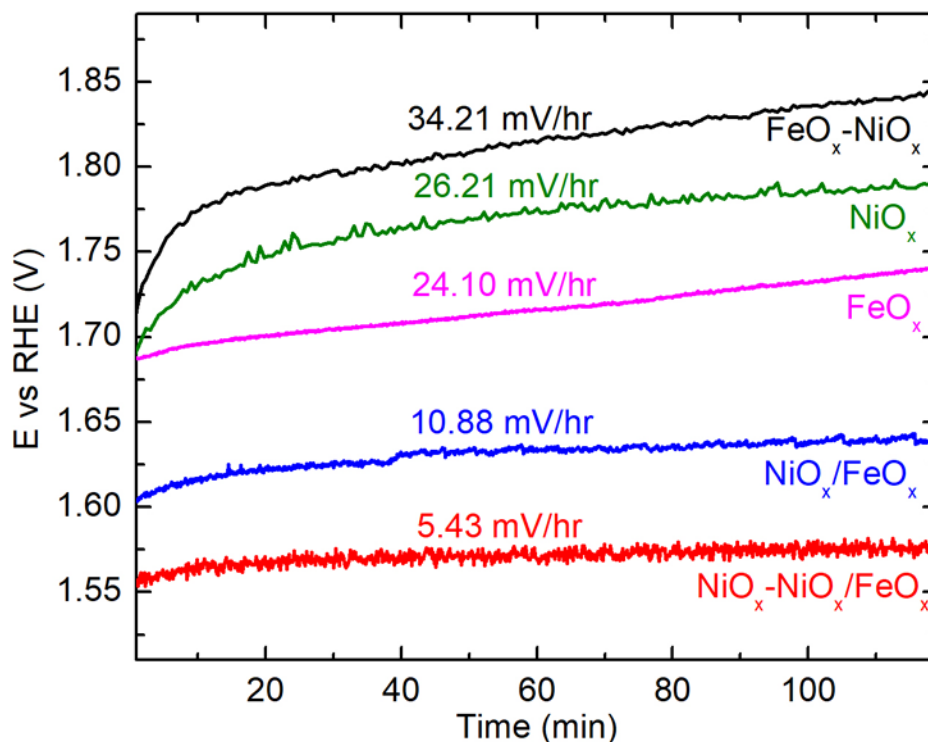
443 in these core-shell nanoparticles. NiO<sub>x</sub>/FeO<sub>x</sub> alloy nanoparticles had the second largest area for the  
444 Ni redox peak and a slight shift to higher voltage of the potential compared to NiO<sub>x</sub> nanoparticles.  
445 Unlike NiO<sub>x</sub> and NiO<sub>x</sub>/FeO<sub>x</sub> alloy nanoparticles, the NiO<sub>x</sub>-NiO<sub>x</sub>/FeO<sub>x</sub> core-mixed shell  
446 nanoparticles had the highest voltage onset for the Ni redox peak, immediately before the onset  
447 potential of OER. The overall trend for the change of the characteristic Ni redox peaks agrees with  
448 previous studies,<sup>19, 65</sup> which concluded that incorporation of Fe in NiO<sub>x</sub> thin films increases the Ni  
449 redox potential and decreases the area of the Ni redox peaks. Further analysis was performed to  
450 calculate the turnover frequency (TOF) based on the quantitative Ni in the samples, where the  
451 amount of Ni was estimated based on either the ICP-MS results or the integration of the redox  
452 wave (i.e., anodic wave) for each of the nanocatalysts. The TOF values for different nanocatalysts  
453 are listed in **Table S2**. For TOF<sub>ICP-MS</sub>, the NiO<sub>x</sub>-NiO<sub>x</sub>/FeO<sub>x</sub> core-mixed shell had the highest value  
454 of 1.175 s<sup>-1</sup>, followed by NiO<sub>x</sub>/FeO<sub>x</sub> alloy with a value of 0.090 s<sup>-1</sup>. The TOF<sub>ICP-MS</sub> values for NiO<sub>x</sub>  
455 and FeO<sub>x</sub>-NiO<sub>x</sub> were 60-80 times lower at 0.006 s<sup>-1</sup> and 0.003 s<sup>-1</sup>, respectively. The TOF<sub>redox wave</sub>  
456 was also calculated with the assumptions of either 1 electron or 1.5 electron transfer per Ni atom.<sup>67</sup>  
457 The TOF<sub>redox wave</sub> values for all of the nanocatalysts were 2-5 times higher than those of the  
458 corresponding TOF<sub>ICP-MS</sub>; however, the trend of both TOF values appeared to be the same in order  
459 of decreasing activity, with NiO<sub>x</sub>-NiO<sub>x</sub>/FeO<sub>x</sub> core-mixed shell > NiO<sub>x</sub>/FeO<sub>x</sub> alloy > NiO<sub>x</sub> ~FeO<sub>x</sub>-  
460 NiO<sub>x</sub>. The TOF values agreed well with the OER activity assessed based on the onset potential of  
461 the benchmark current density of 10 mA/cm<sup>2</sup>.

462 In addition to the electrocatalytic activity, the stability of the nanocatalysts was measured by  
463 chronopotentiometry (CP) for 2 h in 1 M KOH, as shown in **Figure 9**. The degradation rate was  
464 calculated by taking the slope of potential over time for each curve corresponding to each  
465 nanocatalyst. The NiO<sub>x</sub>-NiO<sub>x</sub>/FeO<sub>x</sub> core-mixed shell nanoparticles had the lowest degradation rate

466 of 5.4 mV/h, followed by NiO<sub>x</sub>/FeO<sub>x</sub> alloy nanoparticles at a rate of 10.9 mV/h. The FeO<sub>x</sub>, NiO<sub>x</sub>,  
467 and FeO<sub>x</sub>-NiO<sub>x</sub> had faster degradation rates at 24.1, 26.2, and 34.2 mV/h, respectively. The most  
468 active nanocatalyst (i.e. NiO<sub>x</sub>-NiO<sub>x</sub>/FeO<sub>x</sub> core-mixed shell nanoparticles) was found to be the most  
469 stable electrocatalyst in this series. The NiO<sub>x</sub>/FeO<sub>x</sub> alloy was the second best electrocatalyst based  
470 on the assessment of both activity and stability. The NiO<sub>x</sub>/FeO<sub>x</sub> alloy nanoparticles has a mixed  
471 molar composition of ~0.8:1 (Ni:Fe) while the NiO<sub>x</sub>-NiO<sub>x</sub>/FeO<sub>x</sub> core-mixed shell nanoparticles  
472 contains a pure NiO<sub>x</sub> core and ~0.4:1 (Ni:Fe) mixed alloy shell, but the FeO<sub>x</sub>-NiO<sub>x</sub> core-shell  
473 appeared to be a pure NiO<sub>x</sub> cluster shell (i.e., without any Fe included in the NiO<sub>x</sub> structure). To  
474 our surprise, the NiO<sub>x</sub>-NiO<sub>x</sub>/FeO<sub>x</sub> core-mixed shell nanoparticles, with half the amount of Ni in  
475 the shell compared to the NiO<sub>x</sub>/FeO<sub>x</sub> alloy nanoparticles, out-performed the NiO<sub>x</sub>/FeO<sub>x</sub> alloy  
476 nanoparticles in both activity and stability. Further adding a pure FeO<sub>x</sub> shell increased the onset  
477 potential by 100 mV and thus reduced the electrocatalytic activity (**Figure S10**); and the FeO<sub>x</sub>  
478 core-NiO<sub>x</sub>/FeO<sub>x</sub> mixed shell has similar activity as the NiO<sub>x</sub>/FeO<sub>x</sub> alloy with an onset potential at  
479 1.64 V (**Figure S11**). These results suggest that the mixed NiO<sub>x</sub>/FeO<sub>x</sub> alloy composition is  
480 important to achieve high electrocatalytic activity for OER and the 3-D morphology plays a key  
481 role in optimization of the electrocatalytic activity and stability of the nanocatalyst for OER.

482

483



484  
 485  
 486 **Figure 9.** Chronopotentiometry (CP) of the nanocatalysts obtained in 1 M KOH at a current density  
 487 of 10 mA/cm<sup>2</sup> for 2 h: NiO<sub>x</sub>-NiO<sub>x</sub>/FeO<sub>x</sub> core-mixed shell (red), NiO<sub>x</sub>/FeO<sub>x</sub> alloy (blue), FeO<sub>x</sub>-  
 488 NiO<sub>x</sub> core-shell (black), FeO<sub>x</sub> (pink), and NiO<sub>x</sub> (green).  
 489

#### 490 **Conclusion**

491 In this study, we developed a scalable, oil-based synthesis based on thermal decomposition of  
 492 organometallic complexes that could manipulate both the morphology and crystalline phase of the  
 493 Ni-Fe-based nanocatalysts. Highly uniform Ni-Fe-based nanostructures with different  
 494 morphologies (i.e., Ni-Fe core-shell, Ni/Fe alloy, and Fe-Ni core-shell) were synthesized *via* either  
 495 sequential or simultaneous injection. TEM imaging revealed that the Ni-Fe core-shell was more  
 496 complex due to the diffusion of Ni into the Fe shell, while the Ni-Fe alloy nanoparticle structure  
 497 appeared to be a homogeneous mixture and the Fe-Ni core-shell structure contained an FeO<sub>x</sub> core  
 498 with NiO<sub>x</sub> islands/thin shell. Coupled with x-ray characterization methods on the bulk and surface  
 499 of the sample, we elucidate the morphology, composition, and structure of individual particles for  
 500 each of these nanostructures to be NiO<sub>x</sub>-NiO<sub>x</sub>/FeO<sub>x</sub> core-mixed shell, NiO<sub>x</sub>/FeO<sub>x</sub> alloy, and FeO<sub>x</sub>-

501 NiO<sub>x</sub> core-shell structures. The overpotentials of these nanocatalysts increased in the order of  
502 NiO<sub>x</sub>-NiO<sub>x</sub>/FeO<sub>x</sub> core-mixed shell < NiO<sub>x</sub>/FeO<sub>x</sub> alloy < FeO<sub>x</sub>-NiO<sub>x</sub> core-shell structures ≈ NiO<sub>x</sub> ≈  
503 FeO<sub>x</sub>. The TOF values obtained based on both ICP-MS and redox wave followed the same trend.  
504 These results suggested that the crystalline FeO<sub>x</sub> core did not promote the catalytic activity of NiO<sub>x</sub>  
505 in the FeO<sub>x</sub>-NiO<sub>x</sub> core-shell morphology, possibly due to the high crystallinity of FeO<sub>x</sub>, which  
506 prevented Fe diffusion into the NiO<sub>x</sub> shell. In contrast, the amorphous, disordered nature of the  
507 NiO<sub>x</sub> core, which appears to be most similar to α-Ni(OH)<sub>2</sub>, allowed the diffusion of Ni into the  
508 FeO<sub>x</sub> for the NiO<sub>x</sub>-NiO<sub>x</sub>/FeO<sub>x</sub> core-mixed shell nanoparticles. The resultant mixed metal  
509 hydroxide/oxide shell enabled the most active and stable nanocatalyst, which out-performed the  
510 comparison NiO<sub>x</sub>/FeO<sub>x</sub> alloy nanoparticles with a 1:1 composition expected to be active for OER.  
511 These findings highlight that not only the crystallinity, but also the 3-D morphology, phase, and  
512 chemical environment of both metal species, disorder, and composition, can significantly affect  
513 the electrocatalytic activity and stability of nanocatalysts for alkaline OER.

## 514 **Experimental Methods**

515 **Synthesis of NiO<sub>x</sub>-NiO<sub>x</sub>/FeO<sub>x</sub> Core-Mixed Shell Nanoparticles.** The Ni-Fe core-shell  
516 nanoparticles were synthesized by a two-step procedure involving the synthesis of Ni core and  
517 following by coating the Ni core with Fe shell. In a typical synthesis, Ni(acac)<sub>2</sub> (51.5 mg, 0.2  
518 mmol), 4 mL of octadecene (ODE), and 1 mL of oleylamine (OLAM) were added to a 3-neck,  
519 round bottom flask equipped with a condenser and a Schlenk line system. This reaction mixture  
520 was degassed for 10 min before 1 mL of trioctylphosphine (TOP) was added to the reaction. Under  
521 the protection of argon, the reaction was heated to 220 °C within 10 min and was held at 220 °C  
522 for additional 20 min to allow the formation of Ni cores. The reaction was quenched by removing  
523 the flask from the heating mantle. After the reaction mixture was cooled to 50 °C, the product was

524 transferred to a 50 mL centrifuge tube filled with 5 mL toluene and 20 mL of ethanol which was  
525 centrifuged at 8000 rcf for 5 min to remove excess reactants. The nanoparticle pellet was dispersed  
526 and purified using a mixture of 1:4 toluene and ethanol. The nanoparticles were dispersed in 6 mL  
527 of toluene.

528 For the Fe shelling procedure, 1.8 mL of the above Ni nanoparticles (~5 mg) was dried under  
529 a stream of argon in a 3-neck, round-bottom flask. Then, 200  $\mu$ L of OLAM and 5 mL of ODE  
530 were added to the flask and the nanoparticles were dispersed in the mixture *via* sonication. To  
531 ensure a uniform coating, the reaction temperature was ramped using a step-wise procedure during  
532 the addition of Fe precursor. The temperature was first ramped to 100  $^{\circ}$ C prior to the degassing of  
533 the reaction mixture. The temperature was then continued to ramp to 110  $^{\circ}$ C and held for 10 min.  
534 Then, Fe(CO)<sub>5</sub> (20  $\mu$ L, 0.15 mmol) was injected into the reaction using a gas-tight syringe. After  
535 adding the Fe precursor, the temperature was increased at a rate of 2.5  $^{\circ}$ C/min until 200  $^{\circ}$ C and the  
536 reaction was held at 200  $^{\circ}$ C for 60 min. After the reaction was quenched and cooled to 50  $^{\circ}$ C, the  
537 product was transferred to a 50 mL centrifuge tube filled with ethanol to 30 mL which was  
538 centrifuged at 8000 rcf for 5 min to remove excess reactants. The nanoparticle pellet was dispersed  
539 and purified using a mixture of 2:1 toluene and ethanol and collected by centrifuging at 2000 rcf  
540 for 10 min. The nanoparticles were dispersed in 2 mL of toluene.

541 **Synthesis of Ni-Fe Alloyed Nanoparticles.** Similar procedure was applied to the synthesis of  
542 alloyed nanoparticles as that for the Ni core synthesis except equimolar amounts of Ni(acac)<sub>2</sub> (25.7  
543 mg, 0.1 mmol) and Fe(acac)<sub>3</sub> (26.5 mg, 0.1 mmol) were used in the reaction.

544 **Synthesis of Fe-Ni Core-Shell Nanoparticles.** The Fe-Ni core-shell nanoparticles were  
545 synthesized by a two-step procedure involving the synthesis of Fe core and following by coating  
546 the Fe core with Fe shell. The same reaction set up and heating procedure were used as that for the

547 Ni-Fe core-shell unless specified. In a typical synthesis, Fe(acac)<sub>2</sub> (530.0 mg, 1.5 mmol), 4 mL  
548 of .5 mL of dibenzyl ether (DBE), and 7.5 mL of oleylamine (OLAM) were used in the reaction.  
549 After degassing, the reaction was heated to 280 °C and held at 280 °C for 60 min. The product was  
550 distributed in equal volume into two 50 mL centrifuge tubes filled with ethanol to 30 mL which  
551 was centrifuged at 2000 rcf for 10 min to remove excess reactants. The nanoparticle pellet was  
552 dispersed and purified using a mixture of 1:10 toluene and ethanol twice and collected by  
553 centrifuging at 8000 rcf for 5 min. The nanoparticles were dispersed in 6 mL of toluene.

554 For the Ni shelling procedure, 200 µL of the above Fe nanoparticles (~ 5 mg) was dried under  
555 a stream of argon in a 3-neck, round-bottom flask. Then, 200 µL of OLAM and 5 mL of ODE  
556 were added to the flask and the nanoparticles were dispersed in the mixture *via* sonication. After  
557 degassing, Ni-COD (40.0 mg, 0.15 mmol) added in 2 mL of DBE was injected into the reaction.  
558 The reaction temperature was increased at a rate of 2.5 °C/min to 200 °C and held at 200 °C for 60  
559 min. The product was transferred to a 50 mL centrifuge tube filled with ethanol to 30 mL which  
560 was centrifuged at 8000 rcf for 5 min to remove excess reactants. The nanoparticle pellet was  
561 dispersed and purified using ethanol and collected by centrifuging at 12500 rcf for 10 min. The  
562 nanoparticles were dispersed in 2 mL of toluene.

563 **Nanoparticle Surface Ligand Exchange.** The nanoparticles dispersed in toluene were transferred  
564 into aqueous dispersion by surface ligand exchange process using methoxypolyethylene glycol  
565 carboxylic acid (PEG-COOH, M.W.=5000). In a typical procedure, 2 mL of the nanoparticle  
566 suspension in toluene was added to 10 mL of 1 mg/mL PEG-COOH chloroform solution in a 20  
567 mL scintillation vial. The reaction mixture was capped and stirred overnight. The product was  
568 distributed in two 50 mL centrifuge tubes which were filled to 45 mL with hexane and centrifuged  
569 at 15,000 rcf for 10 min. The resulting pellet was purified with ethanol/water and collected by

570 centrifuging at 20,000 rcf for 30 min at 4 °C. The final product was dispersed in 500 µL of  
571 ethanol/water for quantification and characterization.

572 **Instrumentation.** Low resolution TEM images were captured using a JEOL JEM-1011  
573 microscope with an accelerating voltage of 100 kV. HAADF-STEM images were acquired using  
574 the JEM-ARM200F microscope equipped with cold field emission gun and double aberration  
575 correctors at the accelerating voltage of 200 kV. The inner and outer collection angles for HAADF  
576 images were 67 and 275 mrad, respectively. The spatial resolution of HAADF images was 0.8 Å.  
577 The 2D EELS mapping of Fe L-edge and Ni L-edge was carried out using a Gatan energy-loss  
578 spectrometer at an accelerating voltage of 200 kV and a beam convergence semi-angle of 21.2  
579 mrad. Dispersion of 0.25 eV/channel was used to simultaneously acquire Fe L-edge and Ni L-edge,  
580 as well as O K-edge. The dual-EELS mode was adopted for the convenience of correcting zero-  
581 loss. The mass concentrations of Ni and Fe were determined using a Thermo Scientific iCAP Q  
582 ICP-MS. XRD patterns were collected on Rigaku Ultima III X-ray diffractometer in a parallel  
583 beam geometry. Copper anode x-ray tube was used as a radiation source and diffracted beam  
584 monochromator was employed to remove fluorescence background. Samples were deposited on a  
585 zero diffraction Silicon plates (MTI Corp., CA) and data was collected at 0.07 degrees per minute  
586 scan rates in two theta range from 20 to 80 degrees with 0.1 step. The XPS experiments were  
587 carried out in an ultrahigh vacuum (UHV) system with base pressures  $< 5 \times 10^{-9}$  Torr equipped a  
588 hemispherical electron energy analyzer (SPECS, PHOIBOS 100) and twin anode X-ray source  
589 (SPECS, XR50). Mg  $K_{\alpha}$  (1253.6 eV) radiation was used at 15 kV and 20 mA. The angle between  
590 the analyzer and X-ray source is 45° and photoelectrons were collected along the sample surface  
591 normal. The XPS spectra was analyzed and deconvoluted using Casa XPS software.

592 **X-ray Absorption Spectroscopy.** The XAS of the samples and the standards were performed at  
593 Argonne National Laboratory (APS 12-BM-B). The standards were purchased from commercial  
594 vendors. Standards included nickel foil, nickel oxide, alpha and beta nickel hydroxide, alpha and  
595 gamma nickel oxyhydroxide, iron foil, iron oxides (FeO, Fe<sub>2</sub>O<sub>3</sub>, and Fe<sub>3</sub>O<sub>4</sub>), iron hydroxide, and  
596 iron nickel oxide. Samples and standards were deposited onto the Kapton tape and were sealed on  
597 top by a layer of Kapton tape. Along with the standards and the samples, metal reference foils for  
598 iron and nickel were also ran simultaneously. The data analysis was done through Athena software.  
599 All the standards and the samples were calibrated to the respective metal reference foils. The  
600 measurements were performed at room temperature in transmission mode (or fluorescence mode  
601 with a 13 elements Ge detector). The samples were scanned at the K-edge of Fe (7112 eV) (150  
602 eV below to 800 eV above) and Ni (8333 eV).

603 **Electrochemical Characterization.** The CV and CP were performed on a Pine WaveNow 50  
604 potentiostat using a 3-electrode cell setup. In this setup, Au electrode (BASi®) was used to prepare  
605 the working electrode while a graphite rod was used as the counter electrode and Ag/AgCl (kept  
606 inside a salt bridge containing 3 M NaCl solution) was used as the reference electrode. In all  
607 experiments, 1 M KOH was used as the electrolyte solution. The KOH electrolyte was purified  
608 using the method reported by Trotochaud *et. al.*<sup>68</sup> Argon gas was continuously bubbled throughout  
609 the experiments to remove oxygen formed in the solution.

610 Catalyst inks were prepared by mixing the nanoparticles with a cationic ionomer at a ratio of  
611 6:1 (g Fe: g ionomer) in ethanol. The ink was subsequently sonicated for 15 min to mix the  
612 nanoparticles and the ionomer homogeneously. Approximately 1  $\mu$ l of the ink was deposited onto  
613 the electrode surface (0.02 cm<sup>2</sup>) using the dropcast method and was allowed to dry in air. CV was  
614 run at a scan rate of 10 mV/s between 0 V to 0.8 V vs Ag/AgCl. The data at 21<sup>st</sup> cycle was reported.

615 CP was conducted for 2 h at a current density of 10 mA/cm<sup>2</sup>. Potential in reference to Ag/AgCl  
616 was converted into RHE by using the following equation:  $E_{\text{RHE}} = E_{\text{Ag/AgCl}} + 0.059 \cdot \text{pH} + E^0_{\text{Ag/AgCl}}$ ,  
617 where pH is 14 because the measurement was performed in 1 M KOH;  $E^0_{\text{Ag/AgCl}}$  is 0.21 V for the  
618 reference electrode of Ag/AgCl in 3 M NaCl. The  $iR_u$  correction was applied to the CV curves  
619 obtained from the measurement where  $i$  stands for the measured current in unit ampere and  $R_u$  is  
620 the value of uncompensated resistance.  $R_u$  was measured using potentiostatic electrochemical  
621 impedance spectroscopy and the  $R_u$  values were taken at a frequency of 100 KHz. Calculation  
622 for overpotential was done by subtracting the theoretical potential for OER, 1.23 V, from the  
623 measured potential vs. RHE. To calculate the current density ( $j$ , mA/cm<sup>2</sup>), current is normalized  
624 to geometric surface area of the Au electrode (0.02 cm<sup>2</sup>). Chronopotentiometry was conducted for  
625 2 h at a current density of 10 mA/cm<sup>2</sup>.

## 626 **Supporting Information**

627 Reaction yield and cost estimations; elemental quantifications using electron microscopy;  
628 calculation of turn over frequency; TEM images of NiO<sub>x</sub> nanoparticles; XPS spectra; TEM images  
629 of FeO<sub>x</sub> nanoparticles; XAS spectra of Fe and Ni standards; EXAFS region of Fe and Ni; Table of  
630 TOF values; CV profiles of NiO<sub>x</sub>-NiO<sub>x</sub>/FeO<sub>x</sub> with PEG-HH<sub>2</sub> ligands, NiO<sub>x</sub>-NiO<sub>x</sub>/FeO<sub>x</sub>-FeO<sub>x</sub> and  
631 FeO<sub>x</sub>-NiO<sub>x</sub>/FeO<sub>x</sub>.

## 632 **Author Contribution**

633 JC and LFG designed the experiments and wrote the manuscript. RHM and CCC synthesized the  
634 nanocatalysts. PA performed the electrochemical measurement. DS, JZ, and YZ carried out the  
635 electron microscopy characterization. BR and SL performed the XAS measurement. XT conducted  
636 the XPS measurement. DN obtained the XRD results. All authors contributed to data analysis,  
637 manuscript preparation and editing.

638 **Acknowledgement**

639 We thank Drs. Zhen Wang and Jun Li for the helpful discussion of EELS analysis. JC, LFG, RHM,  
640 and PA gratefully acknowledge funding support from the National Science Foundation (NSF),  
641 Division of Chemical, Bioengineering, Environmental and Transport Systems (CBET) Catalysis  
642 program (Award # 1703827). HRTEM and EELS were carried out at Brookhaven National  
643 Laboratory (BNL) sponsored by the U.S. Department of Energy (DOE) Basic Energy Sciences  
644 (BES) and by the Materials Sciences and Engineering Division under Contract No. DE-  
645 SC0012704. ICP-MS measurements were carried out at the Arkansas Mass Spectrometry facility,  
646 which is supported by the Arkansas Biosciences Institute. XPS and XRD measurements were  
647 performed at the Center for Functional Nanomaterials (CFN), which is a U.S. DOE Office of  
648 Science Facility, at BNL under Contract No. DE-SC0012704. XAS measurements were performed  
649 at the 12-BM beamline at the Advanced Photon Source, a U.S. DOE Office of Science User  
650 Facility operated for the DOE Office of Science by Argonne National Laboratory under Contract  
651 DE-AC02-06CH11357.

652

653

654 **References**

- 655 1. Zeng, K.; Zhang, D., Recent progress in alkaline water electrolysis for hydrogen production  
656 and applications. *Progress in Energy and Combustion Science* **2010**, *36* (3), 307-326.
- 657 2. Carmo, M.; Fritz, D. L.; Mergel, J.; Stolten, D., A comprehensive review on PEM water  
658 electrolysis. *International Journal of Hydrogen Energy* **2013**, *38* (12), 4901-4934.
- 659 3. Reier, T.; Nong, H. N.; Teschner, D.; Schlögl, R.; Strasser, P., Electrocatalytic Oxygen  
660 Evolution Reaction in Acidic Environments – Reaction Mechanisms and Catalysts. *Advanced*  
661 *Energy Materials* **2017**, *7* (1), 1601275-n/a.
- 662 4. Ma, Z.; Zhang, Y.; Liu, S.; Xu, W.; Wu, L.; Hsieh, Y.-C.; Liu, P.; Zhu, Y.; Sasaki, K.;  
663 Renner, J. N.; Ayers, K. E.; Adzic, R. R.; Wang, J. X., Reaction mechanism for oxygen  
664 evolution on RuO<sub>2</sub>, IrO<sub>2</sub>, and RuO<sub>2</sub>@IrO<sub>2</sub> core-shell nanocatalysts. *Journal of*  
665 *Electroanalytical Chemistry* **2018**, *819*, 296-305.
- 666 5. Reier, T.; Oezaslan, M.; Strasser, P., Electrocatalytic Oxygen Evolution Reaction (OER) on  
667 Ru, Ir, and Pt Catalysts: A Comparative Study of Nanoparticles and Bulk Materials. *ACS*  
668 *Catal.* **2012**, *2* (8), 1765-1772.
- 669 6. Lee, Y.; Suntivich, J.; May, K. J.; Perry, E. E.; Shao-Horn, Y., Synthesis and Activities of  
670 Rutile IrO<sub>2</sub> and RuO<sub>2</sub> Nanoparticles for Oxygen Evolution in Acid and Alkaline Solutions.  
671 *The Journal of Physical Chemistry Letters* **2012**, *3* (3), 399-404.
- 672 7. McCrory, C. C.; Jung, S.; Peters, J. C.; Jaramillo, T. F., Benchmarking heterogeneous  
673 electrocatalysts for the oxygen evolution reaction. *Journal of the American Chemical Society*  
674 **2013**, *135* (45), 16977-16987.
- 675 8. Matsumoto, Y.; Sato, E., Electrocatalytic properties of transition metal oxides for oxygen  
676 evolution reaction. *Materials Chemistry and Physics* **1986**, *14* (5), 397-426.
- 677 9. Man, I. C.; Su, H.-Y.; Calle-Vallejo, F.; Hansen, H. A.; Martínez, J. I.; Inoglu, N. G.;  
678 Kitchin, J.; Jaramillo, T. F.; Nørskov, J. K.; Rossmeisl, J., Universality in Oxygen Evolution  
679 Electrocatalysis on Oxide Surfaces. *ChemCatChem* **2011**, *3* (7), 1159-1165.
- 680 10. Burke, M. S.; Enman, L. J.; Batchellor, A. S.; Zou, S.; Boettcher, S. W., Oxygen Evolution  
681 Reaction Electrocatalysis on Transition Metal Oxides and (Oxy)hydroxides: Activity Trends  
682 and Design Principles. *Chemistry of Materials* **2015**, *27* (22), 7549-7558.
- 683 11. Fabbri, E.; Habereder, A.; Waltar, K.; Kötz, R.; Schmidt, T. J., Developments and  
684 perspectives of oxide-based catalysts for the oxygen evolution reaction. *Catalysis Science &*  
685 *Technology* **2014**, *4* (11), 3800-3821.
- 686 12. Kim, J. S.; Kim, B.; Kim, H.; Kang, K., Recent Progress on Multimetal Oxide Catalysts for  
687 the Oxygen Evolution Reaction. *Advanced Energy Materials* **2018**, *8* (11), 1702774.
- 688 13. Burke, M. S.; Zou, S.; Enman, L. J.; Kellon, J. E.; Gabor, C. A.; Pledger, E.; Boettcher, S.  
689 W., Revised Oxygen Evolution Reaction Activity Trends for First-Row Transition-Metal  
690 (Oxy)hydroxides in Alkaline Media. *The Journal of Physical Chemistry Letters* **2015**, *6* (18),  
691 3737-3742.
- 692 14. Gong, M.; Dai, H., A mini review of NiFe-based materials as highly active oxygen evolution  
693 reaction electrocatalysts. *Nano Res.* **2015**, *8* (1), 23-39.
- 694 15. Dionigi, F.; Strasser, P., NiFe-Based (Oxy)hydroxide Catalysts for Oxygen Evolution  
695 Reaction in Non-Acidic Electrolytes. *Advanced Energy Materials* **2016**, *6* (23), 1600621.
- 696 16. Tichenor, R. L., Nickel Oxides-Relation Between Electrochemical and Foreign Ion Content.  
697 *Industrial & Engineering Chemistry* **1952**, *44* (5), 973-977.

- 698 17. Młynarek, G.; Paszkiewicz, M.; Radniecka, A., The effect of ferric ions on the behaviour of a  
699 nickelous hydroxide electrode. *Journal of applied electrochemistry* **1984**, *14* (2), 145-149.
- 700 18. Corrigan, D. A., The catalysis of the oxygen evolution reaction by iron impurities in thin-film  
701 nickel-oxide electrodes. *Journal of the Electrochemical Society* **1987**, *134* (2), 377-384.
- 702 19. Trotochaud, L.; Young, S. L.; Ranney, J. K.; Boettcher, S. W., Nickel-iron oxyhydroxide  
703 oxygen-evolution electrocatalysts: The role of intentional and incidental iron incorporation.  
704 *J. Am. Chem. Soc.* **2014**, *136*, 6744-6753.
- 705 20. Klaus, S.; Louie, M. W.; Trotochaud, L.; Bell, A. T., Role of Catalyst Preparation on the  
706 Electrocatalytic Activity of Ni<sub>1-x</sub>Fe<sub>x</sub>OOH for the Oxygen Evolution Reaction. *The Journal*  
707 *of Physical Chemistry C* **2015**, *119* (32), 18303-18316.
- 708 21. Ahn, H. S.; Bard, A. J., Surface Interrogation Scanning Electrochemical Microscopy of Ni<sub>1-</sub>  
709 <sub>x</sub>Fe<sub>x</sub>OOH (0 < x < 0.27) Oxygen Evolving Catalyst: Kinetics of the “fast” Iron Sites. *Journal*  
710 *of the American Chemical Society* **2016**, *138* (1), 313-318.
- 711 22. Görlin, M.; Chernev, P.; Ferreira de Araújo, J.; Reier, T.; Dresp, S.; Paul, B.; Krähnert, R.;  
712 Dau, H.; Strasser, P., Oxygen Evolution Reaction Dynamics, Faradaic Charge Efficiency,  
713 and the Active Metal Redox States of Ni-Fe Oxide Water Splitting Electrocatalysts. *Journal*  
714 *of the American Chemical Society* **2016**, *138* (17), 5603-5614.
- 715 23. Görlin, M.; Ferreira de Araújo, J.; Schmies, H.; Bernsmeier, D.; Dresp, S.; Gliech, M.; Jusys,  
716 Z.; Chernev, P.; Kraehnert, R.; Dau, H.; Strasser, P., Tracking Catalyst Redox States and  
717 Reaction Dynamics in Ni-Fe Oxyhydroxide Oxygen Evolution Reaction Electrocatalysts:  
718 The Role of Catalyst Support and Electrolyte pH. *Journal of the American Chemical Society*  
719 **2017**, *139* (5), 2070-2082.
- 720 24. Li, N.; Bediako, D. K.; Hadt, R. G.; Hayes, D.; Kempa, T. J.; von Cube, F.; Bell, D. C.;  
721 Chen, L. X.; Nocera, D. G., Influence of iron doping on tetravalent nickel content in catalytic  
722 oxygen evolving films. *Proceedings of the National Academy of Sciences* **2017**, *114* (7),  
723 1486-1491.
- 724 25. Stevens, M. B.; Trang, C. D. M.; Enman, L. J.; Deng, J.; Boettcher, S. W., Reactive Fe-Sites  
725 in Ni/Fe (Oxy)hydroxide Are Responsible for Exceptional Oxygen Electrocatalysis Activity.  
726 *Journal of the American Chemical Society* **2017**, *139* (33), 11361-11364.
- 727 26. Corrigan, D. A.; Conell, R. S.; Fierro, C. A.; Scherson, D. A., In-situ Moessbauer study of  
728 redox processes in a composite hydroxide of iron and nickel. *The Journal of Physical*  
729 *Chemistry* **1987**, *91* (19), 5009-5011.
- 730 27. Guerlou-Demourgues, L.; Fournès, L.; Delmas, C., In Situ <sup>57</sup>Fe Mössbauer Spectroscopy  
731 Study of the Electrochemical Behavior of an Iron-Substituted Nickel Hydroxide Electrode.  
732 *Journal of The Electrochemical Society* **1996**, *143* (10), 3083-3088.
- 733 28. Chen, J. Y. C.; Dang, L.; Liang, H.; Bi, W.; Gerken, J. B.; Jin, S.; Alp, E. E.; Stahl, S. S.,  
734 Operando Analysis of NiFe and Fe Oxyhydroxide Electrocatalysts for Water Oxidation:  
735 Detection of Fe<sup>4+</sup> by Mössbauer Spectroscopy. *Journal of the American Chemical Society*  
736 **2015**, *137* (48), 15090-15093.
- 737 29. Louie, M. W.; Bell, A. T., An investigation of thin-film Ni-Fe oxide catalysts for the  
738 electrochemical evolution of oxygen. *Journal of the American Chemical Society* **2013**, *135*  
739 (33), 12329-12337.
- 740 30. Klaus, S.; Cai, Y.; Louie, M. W.; Trotochaud, L.; Bell, A. T., Effects of Fe Electrolyte  
741 Impurities on Ni(OH)<sub>2</sub>/NiOOH Structure and Oxygen Evolution Activity. *The Journal of*  
742 *Physical Chemistry C* **2015**, *119* (13), 7243-7254.

- 743 31. Steimecke, M.; Seiffarth, G.; Bron, M., In Situ Characterization of Ni and Ni/Fe Thin Film  
744 Electrodes for Oxygen Evolution in Alkaline Media by a Raman-Coupled Scanning  
745 Electrochemical Microscope Setup. *Analytical Chemistry* **2017**, *89* (20), 10679-10686.
- 746 32. Kim, S.; Tryk, D. A.; Antonio, M. R.; Carr, R.; Scherson, D., In situ x-ray absorption fine  
747 structure studies of foreign metal ions in nickel hydrous oxide electrodes in alkaline  
748 electrolytes. *The Journal of Physical Chemistry* **1994**, *98* (40), 10269-10276.
- 749 33. Balasubramanian, M.; Melendres, C. A.; Mini, S., X-ray Absorption Spectroscopy Studies of  
750 the Local Atomic and Electronic Structure of Iron Incorporated into Electrodeposited  
751 Hydrous Nickel Oxide Films. *The Journal of Physical Chemistry B* **2000**, *104* (18), 4300-  
752 4306.
- 753 34. Landon, J.; Demeter, E.; İnoğlu, N.; Keturakis, C.; Wachs, I. E.; Vasić, R.; Frenkel, A. I.;  
754 Kitchin, J. R., Spectroscopic Characterization of Mixed Fe–Ni Oxide Electrocatalysts for the  
755 Oxygen Evolution Reaction in Alkaline Electrolytes. *ACS Catal.* **2012**, *2* (8), 1793-1801.
- 756 35. Trześniewski, B. J.; Diaz-Morales, O.; Vermaas, D. A.; Longo, A.; Bras, W.; Koper, M. T.  
757 M.; Smith, W. A., In Situ Observation of Active Oxygen Species in Fe-Containing Ni-Based  
758 Oxygen Evolution Catalysts: The Effect of pH on Electrochemical Activity. *Journal of the*  
759 *American Chemical Society* **2015**, *137* (48), 15112-15121.
- 760 36. Friebel, D.; Louie, M. W.; Bajdich, M.; Sanwald, K. E.; Cai, Y.; Wise, A. M.; Cheng, M.-J.;  
761 Sokaras, D.; Weng, T.-C.; Alonso-Mori, R.; Davis, R. C.; Bargar, J. R.; Nørskov, J. K.;  
762 Nilsson, A.; Bell, A. T., Identification of Highly Active Fe Sites in (Ni,Fe)OOH for  
763 Electrocatalytic Water Splitting. *Journal of the American Chemical Society* **2015**, *137* (3),  
764 1305-1313.
- 765 37. Bates, M. K.; Jia, Q.; Doan, H.; Liang, W.; Mukerjee, S., Charge-Transfer Effects in Ni–Fe  
766 and Ni–Fe–Co Mixed-Metal Oxides for the Alkaline Oxygen Evolution Reaction. *ACS Catal.*  
767 **2016**, *6* (1), 155-161.
- 768 38. González-Flores, D.; Klingan, K.; Chernev, P.; Loos, S.; Mohammadi, M. R.; Pasquini, C.;  
769 Kubella, P.; Zaharieva, I.; Smith, R. D.; Dau, H., Nickel-iron catalysts for electrochemical  
770 water oxidation–redox synergism investigated by in situ X-ray spectroscopy with millisecond  
771 time resolution. *Sustainable Energy & Fuels* **2018**.
- 772 39. Smith, R. D.; Pasquini, C.; Loos, S.; Chernev, P.; Klingan, K.; Kubella, P.; Mohammadi, M.  
773 R.; González-Flores, D.; Dau, H., Geometric distortions in nickel (oxy) hydroxide  
774 electrocatalysts by redox inactive iron ions. *Energy & Environmental Science* **2018**.
- 775 40. Li, Y.-F.; Selloni, A., Mechanism and Activity of Water Oxidation on Selected Surfaces of  
776 Pure and Fe-Doped NiOx. *ACS Catal.* **2014**, *4* (4), 1148-1153.
- 777 41. Conesa, J. C., Electronic Structure of the (Undoped and Fe-Doped) NiOOH O<sub>2</sub> Evolution  
778 Electrocatalyst. *The Journal of Physical Chemistry C* **2016**, *120* (34), 18999-19010.
- 779 42. Xiao, H.; Shin, H.; Goddard, W. A., Synergy between Fe and Ni in the optimal performance  
780 of (Ni,Fe)OOH catalysts for the oxygen evolution reaction. *Proceedings of the National*  
781 *Academy of Sciences* **2018**, *115* (23), 5872-5877.
- 782 43. Kuai, L.; Geng, J.; Chen, C.; Kan, E.; Liu, Y.; Wang, Q.; Geng, B., A Reliable Aerosol-  
783 Spray-Assisted Approach to Produce and Optimize Amorphous Metal Oxide Catalysts for  
784 Electrochemical Water Splitting. *Angewandte Chemie International Edition* **2014**, *53* (29),  
785 7547-7551.
- 786 44. Song, F.; Hu, X., Exfoliation of layered double hydroxides for enhanced oxygen evolution  
787 catalysis. *Nat Commun* **2014**, *5*.

- 788 45. Deng, J.; Nellist, M. R.; Stevens, M. B.; Dette, C.; Wang, Y.; Boettcher, S. W., Morphology  
789 Dynamics of Single-Layered Ni(OH)<sub>2</sub>/NiOOH Nanosheets and Subsequent Fe Incorporation  
790 Studied by in Situ Electrochemical Atomic Force Microscopy. *Nano Letters* **2017**.
- 791 46. Dette, C.; Hurst, M. R.; Deng, J.; Nellist, M. R.; Boettcher, S. W., Structural Evolution of  
792 Metal (Oxy)hydroxide Nanosheets during the Oxygen Evolution Reaction. *ACS Applied*  
793 *Materials & Interfaces* **2018**.
- 794 47. Huang, J.; Han, J.; Wang, R.; Zhang, Y.; Wang, X.; Zhang, X.; Zhang, Z.; Zhang, Y.; Song,  
795 B.; Jin, S., Improving Electrocatalysts for Oxygen Evolution Using Ni<sub>x</sub>Fe<sub>3-x</sub>O<sub>4</sub>/Ni Hybrid  
796 Nanostructures Formed by Solvothermal Synthesis. *ACS Energy Letters* **2018**, 3 (7), 1698-  
797 1707.
- 798 48. Candelaria, S. L.; Bedford, N. M.; Woehl, T. J.; Rentz, N. S.; Showalter, A. R.; Pylypenko,  
799 S.; Bunker, B. A.; Lee, S.; Reinhart, B.; Ren, Y.; Ertem, S. P.; Coughlin, E. B.; Sather, N. A.;  
800 Horan, J. L.; Herring, A. M.; Greenlee, L. F., Multi-Component Fe–Ni Hydroxide  
801 Nanocatalyst for Oxygen Evolution and Methanol Oxidation Reactions under Alkaline  
802 Conditions. *ACS Catal.* **2017**, 7 (1), 365-379.
- 803 49. Hall, D. S.; Lockwood, D. J.; Bock, C.; MacDougall, B. R., Nickel hydroxides and related  
804 materials: a review of their structures, synthesis and properties. *Proceedings. Mathematical,*  
805 *Physical, and Engineering Sciences / The Royal Society* **2015**, 471 (2174), 20140792.
- 806 50. Gao, M.; Sheng, W.; Zhuang, Z.; Fang, Q.; Gu, S.; Jiang, J.; Yan, Y., Efficient Water  
807 Oxidation Using Nanostructured  $\alpha$ -Nickel-Hydroxide as an Electrocatalyst. *Journal of the*  
808 *American Chemical Society* **2014**, 136 (19), 7077-7084.
- 809 51. Sun, S.; Zeng, H.; Robinson, D. B.; Raoux, S.; Rice, P. M.; Wang, S. X.; Li, G.,  
810 Monodisperse MFe<sub>2</sub>O<sub>4</sub> (M = Fe, Co, Mn) Nanoparticles. *Journal of the American Chemical*  
811 *Society* **2004**, 126 (1), 273-279.
- 812 52. Chen, S.; Si, R.; Taylor, E.; Janzen, J.; Chen, J., Synthesis of Pd/Fe<sub>3</sub>O<sub>4</sub> Hybrid  
813 Nanocatalysts with Controllable Interface and Enhanced Catalytic Activities for CO  
814 Oxidation. *The Journal of Physical Chemistry C* **2012**, 116 (23), 12969-12976.
- 815 53. Balasubramanian, M.; Melendres, C. A.; Mini, S., X-ray absorption spectroscopy studies of  
816 the local atomic and electronic structure of iron incorporated into electrodeposited hydrous  
817 nickel oxide films. *J. Phys. Chem. B* **2000**, 104, 4300-4306.
- 818 54. Brollo, M. E. F.; López-Ruiz, R.; Muraca, D.; Figueroa, S. J. A.; Pirota, K. R.; Knobel, M.,  
819 Compact Ag@Fe<sub>3</sub>O<sub>4</sub> Core-shell Nanoparticles by Means of Single-step Thermal  
820 Decomposition Reaction. *Scientific Reports* **2014**, 4, 6839.
- 821 55. Hartl, M.; Gillis, R. C.; Daemen, L.; Olds, D. P.; Page, K.; Carlson, S.; Cheng, Y.; Hügler, T.;  
822 Iverson, E. B.; Ramirez-Cuesta, A. J.; Lee, Y.; Muhrer, G., Hydrogen adsorption on two  
823 catalysts for the ortho- to parahydrogen conversion: Cr-doped silica and ferric oxide gel.  
824 *Physical Chemistry Chemical Physics* **2016**, 18 (26), 17281-17293.
- 825 56. Chen, J. Y. C.; Miller, J. T.; Gerken, J. B.; Stahl, S. S., Inverse spinel NiFeAlO<sub>4</sub> as a highly  
826 active oxygen evolution electrocatalyst: promotion of activity by a redox-inert metal ion.  
827 *Energy & Environmental Science* **2014**, 7 (4), 1382-1386.
- 828 57. Chen, C. L.; Dong, C.-L., X-Ray Spectroscopy Studies of Iron Chalcogenides. In  
829 *Superconductors - Materials, Properties and Applications*, Gabovich, A., Ed. InTech: Rijeka,  
830 2012; p Ch. 02.
- 831 58. Regan, T. J.; Ohldag, H.; Stamm, C.; Nolting, F.; Lüning, J.; Stöhr, J.; White, R. L.,  
832 Chemical effects at metal/oxide interfaces studied by x-ray-absorption spectroscopy.  
833 *Physical Review B* **2001**, 64 (21), 214422.

- 834 59. Chen, T.; Cao, L.; Zhang, W.; Zhang, W.; Han, Y.; Zheng, Z.; Xu, F.; Kurash, I.; Qian, H.;  
835 Wang, J. o., Correlation between electronic structure and magnetic properties of Fe-doped  
836 ZnO films. *Journal of Applied Physics* **2012**, *111* (12), 123715.
- 837 60. Kim, D. H.; Lee, H. J.; Kim, G.; Koo, Y. S.; Jung, J. H.; Shin, H. J.; Kim, J. Y.; Kang, J. S.,  
838 Interface electronic structures of BaTiO<sub>3</sub>@X nanoparticles (X= g-Fe<sub>2</sub>O<sub>3</sub>, Fe<sub>3</sub>O<sub>4</sub>, a-Fe<sub>2</sub>O<sub>3</sub>, and  
839 Fe) investigated by XAS and XMCD. *Physical Review B* **2009**, *79* (3), 033402.
- 840 61. van Aken, P. A.; Liebscher, B., Quantification of ferrous/ferric ratios in minerals: new  
841 evaluation schemes of Fe L23electron energy-loss near-edge spectra. *Physics and Chemistry  
842 of Minerals* **2002**, *29* (3), 188-200.
- 843 62. Tan, H.; Verbeeck, J.; Abakumov, A.; Van Tendeloo, G., Oxidation state and chemical shift  
844 investigation in transition metal oxides by EELS. *Ultramicroscopy* **2012**, *116*, 24-33.
- 845 63. Chen, J.; Huang, D. J.; Tanaka, A.; Chang, C. F.; Chung, S. C.; Wu, W. B.; Chen, C. T.,  
846 Magnetic circular dichroism in Fe 2p resonant photoemission of magnetite. *Physical Review  
847 B* **2004**, *69* (8), 085107.
- 848 64. Zhao, W.; Li, M.; Chang, C.-Z.; Jiang, J.; Wu, L.; Liu, C.; Moodera, J. S.; Zhu, Y.; Chan, M.  
849 H. W., Direct imaging of electron transfer and its influence on superconducting pairing at  
850 FeSe/SrTiO<sub>3</sub> interface. *Science Advances* **2018**, *4* (3).
- 851 65. Klaus, S.; Cai, Y.; Louie, M. W.; Trotochaud, L.; Bell, A. T., Effects of Fe electrolyte  
852 impurities on Ni(OH)<sub>2</sub>/NiOOH structure and oxygen evolution activity. *J. Phys. Chem. C*  
853 **2015**, *119*, 7243-7254.
- 854 66. Bau, J. A.; Lubner, E. J.; Buriak, J. M., Oxygen Evolution Catalyzed by Nickel–Iron Oxide  
855 Nanocrystals with a Nonequilibrium Phase. *ACS Applied Materials & Interfaces* **2015**, *7*  
856 (35), 19755-19763.
- 857 67. Smith, R. D. L.; Berlinguette, C. P., Accounting for the Dynamic Oxidative Behavior of  
858 Nickel Anodes. *Journal of the American Chemical Society* **2016**, *138* (5), 1561-1567.
- 859 68. Trotochaud, L.; Young, S. L.; Ranney, J. K.; Boettcher, S. W., Nickel–Iron Oxyhydroxide  
860 Oxygen-Evolution Electrocatalysts: The Role of Intentional and Incidental Iron  
861 Incorporation. *Journal of the American Chemical Society* **2014**, *136* (18), 6744-6753.

862

## Supporting Information

### Controlling 3-D Morphology of Ni-Fe-Based Nanocatalysts for Oxygen Evolution Reaction

Ryan Manso,<sup>1,†</sup> Prashant Acharya,<sup>2,†</sup> Shiqing Deng,<sup>3,4†</sup> Cameron C. Crane,<sup>1</sup> Benjamin Reinhart,<sup>5</sup>  
Sungsik Lee,<sup>5</sup> Xiao Tong,<sup>6</sup> Dmytro Nykypanchuk,<sup>6</sup> Jing Zhu,<sup>4</sup> Yimei Zhu,<sup>3</sup> Lauren F.  
Greenlee,<sup>2,\*</sup> and Jingyi Chen<sup>1,\*</sup>

<sup>1</sup>Department of Chemistry and Biochemistry, University of Arkansas, Fayetteville, AR 72701,  
USA

<sup>2</sup>Ralph E. Martin Department of Chemical Engineering, University of Arkansas, Fayetteville, AR  
72701, USA

<sup>3</sup>Condensed Matter Physics and Materials Science Department, Brookhaven National  
Laboratory, Upton, NY 11973, USA

<sup>4</sup>School of Materials Science and Engineering, Tsinghua University, Beijing 100084, P. R. China

<sup>5</sup>Advanced Photon Source, Argonne National Laboratory, Lemont, IL 60439, USA

<sup>6</sup>Center for Functional Nanomaterials, Brookhaven National Laboratory, Upton, NY 11973, USA

<sup>†</sup>These authors contributed to this work equally.

\*Corresponding authors: chenj@uark.edu (synthesis, characterization) and greenlee@uark.edu  
(electrocatalysis, characterization)

**Reaction Yield and Cost Estimations.** We used our best performing catalyst as an example to calculate the yield of synthesis and estimate the cost of the small scale synthesis. The synthesis involves 3 steps: step 1 - synthesis of NiO<sub>x</sub> cores; step 2 - shelling with FeO<sub>x</sub>; and step 3 - ligand exchange from oleylamine to PEG-COOH. The amount of Ni for each step was quantitatively measured by ICP-MS and used to calculate the reaction yield. The yield of each step was calculated using the actual measured value divided by the theoretical value from the reaction and reported as percentage yield. For step 1, the yield is >95% after purification. The high yield of NiO<sub>x</sub> is the result of two factors: 1) the reaction is performed under relatively-high temperature that can drive the reaction nearly completion; and 2) the nanoparticle self-assembly effect due to their hydrophobic ligands is quite effective to collect all the nanoparticles during centrifugation purification. The yield for the shelling is ~90%, but the overall yield is ~60%. The major cause of the loss in the overall yield comes from the relatively-low recovery from the centrifugation after the particle surface is covered with water soluble ligands. This loss can be minimized by using filter centrifuge tubes with a molecular cutoff slightly larger than the molar mass of the ligands (e.g. 10,000 Da) or a combination of dialysis and lyophilization to remove excess ligands and then water.

The cost estimation of the small scale synthesis is listed below in **Table S1** for the three-step synthesis. Each synthesis yields ~7 mg catalysts for the cost of ~\$2.76, roughly ~\$0.4/mg. Similar small-scale synthesis for 10 mg Ir by simply reacting IrCl<sub>3</sub> (\$261.00/1g, Alfa Aesar) with NaBH<sub>4</sub> will cost about the same \$0.4/mg if assuming 100% yield. However, our 3-step synthesis has room to bring down the cost by optimizing the process. For example, we can eliminate the purification procedure before Fe shelling step because step 1 nearly 100% converts the Ni precursor to NiO<sub>x</sub>. As the 3-step process becomes 2 step, the yield of the reaction can be improved by at least 10%.

We can further improve the yield of purification process mentioned above. It is expected that we can improve the overall yield of the reaction to ~90% that will bring down the cost to ~0.3/mg. The price can be further reduced by using less solvent due to reduction of reaction steps and using a cheaper ligand (i.e. poly(acrylic acid), \$45.80/5 g) or potentially replacing the ligand exchange process by other methods. Therefore, we estimate that the cost of small scale process can be reduced to 1/3 or 1/4 of the original price at ~\$0.1/mg. In the case of noble metal, there is not much room to lower the production cost because the overall price is limited by the source of noble metal precursors. Thus, we consider the catalysts are low-cost and viable for future development. As for scale up production, similar to all other chemical synthesis, the solution-based synthesis of our catalysts at a large scale or gram scale is feasible by either scaling up the batch synthesis or using flow chemistry. When the production is scaled up, the price will be significantly reduced as it can be seen in the industries from chemical to pharmaceutical productions.

**Table S1.** The estimated cost per small scale 3-step synthesis for NiO<sub>x</sub>-NiO<sub>x</sub>/FeO<sub>x</sub> core-shell nanocatalysts

Chemicals	Price	Amount used/synthesis	Price/synthesis
Ni(acac) <sub>2</sub>	\$39.70/25 g (Alfa Aesar)	51.5 mg	\$0.08
Octadecene	\$33.03/1 L (Acros)	9 mL	\$0.30
Oleylamine	\$132.00/500 g (Sigma-Aldrich)	1.2 mL	\$0.32
Trioctylphosphine	\$42.71/100 mL (Alfa Aesar)	1 mL	\$0.43
Fe(CO) <sub>5</sub>	\$35.10/25 g (Alfa Aesar)	20 uL	\$0.03
PEG-COOH	\$800.00/10 g (JenKem)	10 mg	\$0.80
Toluene*	\$120/19 L (VWR)	10 mL	\$0.06
Ethanol*	\$23.85/3.8 L (KOPTEC)	50 mL	\$0.31
Chloroform*	\$21.42/1 L (VWR)	10 mL	\$0.21
Hexane*	\$94.79/19 L (VWR)	45 mL	\$0.22
Total			\$2.76

**Elemental Quantifications using Electron Microscopy.**<sup>1</sup> Elemental quantifications were performed on the 2D maps of Fe L<sub>2,3</sub> edge and Ni L<sub>2,3</sub> edge using EELS QUANTIFICATION plug-in in Digital Micrograph commercial software. The quantitative analysis is based on the

fundamental relationship, given by  $I_k = NI_0\sigma_k$ , where  $I_0$  represents the unscattered (zero-loss) intensity and  $N$  is the areal concentration (atoms /nm<sup>2</sup>) of the element contributing to the ionization edge  $k$ ,  $I_k$  is the sum of all counts in that edge, and  $\sigma_k$  is the cross-section for ionization. Considering that a certain fraction of the electrons is intercepted by the angle-limiting aperture, partial cross-section  $\sigma_k(\beta, \Delta)$  for energy losses within a range of the ionization threshold and for scattering angles up to  $\beta$  the above relationship should be used in the above relationship.  $\beta$  and  $\Delta$  represent the scattering capture semi-angle angle (10.42 mrad) and signal integration width, respectively. After removing plural scattering from spectra *via* Fourier-Log deconvolution, atomic ratios of two elements (Ni and Fe) can be determined by

$$R_{Ni/Fe} = \frac{N_{Ni}}{N_{Fe}} = \frac{I_{LNi}^1(\beta, \Delta_{Ni}) \sigma_{LFe}(\beta, \Delta_{Fe}) F_{1Fe}}{I_{LFe}^1(\beta, \Delta_{Fe}) \sigma_{LNi}(\beta, \Delta_{Ni}) F_{1Ni}},$$

where  $\Delta_{Fe} = \Delta_{Ni} = 40$  eV,  $\sigma_{LNi}(\beta, \Delta)$  and  $\sigma_{LFe}(\beta, \Delta)$  are partial cross-sections of Ni and Fe, respectively. In this algorithm, partial cross-sections are determined by calculating the energy-differential cross-section,  $d\sigma/dE$ , for the L-edge and integrates it over the specified signal integration energy-range. Hartree-Slater model was used for calculations. Based on our setups,  $\sigma_{LNi}(\beta, \Delta)$  and  $\sigma_{LFe}(\beta, \Delta)$  were determined as  $310 \pm 31$  barns and  $194 \pm 19$  barns (A barn is  $10^{-28}$  m<sup>2</sup>), respectively.  $F_{1Fe}/F_{1Ni}$  is used to correct the incident beam convergence, which was computed at each  $d\sigma/dE$ .

**Calculation of turn over frequency (TOF).** The TOF was calculated based on the protocol established in the work of Stevens *et.al.*<sup>2</sup> TOF is defined in eq. 1.

$$\text{TOF} = \frac{\frac{\text{current}}{4F}}{\text{mol active sites}} \quad (1)$$

where  $F$  is Faraday's constant. The value for current was read at an overpotential of 400 mV and Ni atoms is considered as the active sites. The amount of Ni active sites on the electrode surface was estimated based on either ICP-MS analysis ( $\text{TOF}_{\text{ICP-MS}}$ ) or redox wave ( $\text{TOF}_{\text{redox wave}}$ ). For the former, the number of Ni active sites in moles is the amount of Ni placed on the electrode based on data obtained from ICP-MS. For the latter, the number of Ni active sites  $N$  is based on the amount of charge  $Q$  in coulombs (C) involved in the anodic wave using eq. 2.

$$N = \frac{Q}{mF} \quad (2)$$

where  $m$  is number of electrons transferred for the anodic reaction of Ni and  $F$  is Faraday's constant. Based on literature,  $\text{TOF}_{\text{redox wave}}$  were calculated based on the assumption of either  $1e^-$  transfer or  $1.5e^-$  transfer, thereby  $m$  being either 1 or 1.5 in our calculation.<sup>2,3</sup> The charge  $Q$  involved in the anodic reaction of Ni can be calculated using eq. 3.

$$Q = \frac{1}{\nu} \int IdE \quad (3)$$

where  $\nu$  is the scan rate in V/s,  $I$  is current in amperes (A), and  $E$  is potential in volts (V). The value for  $\int IdE$  was obtained by integrating anodic peak of Ni in the CV curve of the corresponding catalyst. The integration was not compensated with uncompensated resistance during data collection such that the current magnitude has no dependence on the sweep rate.

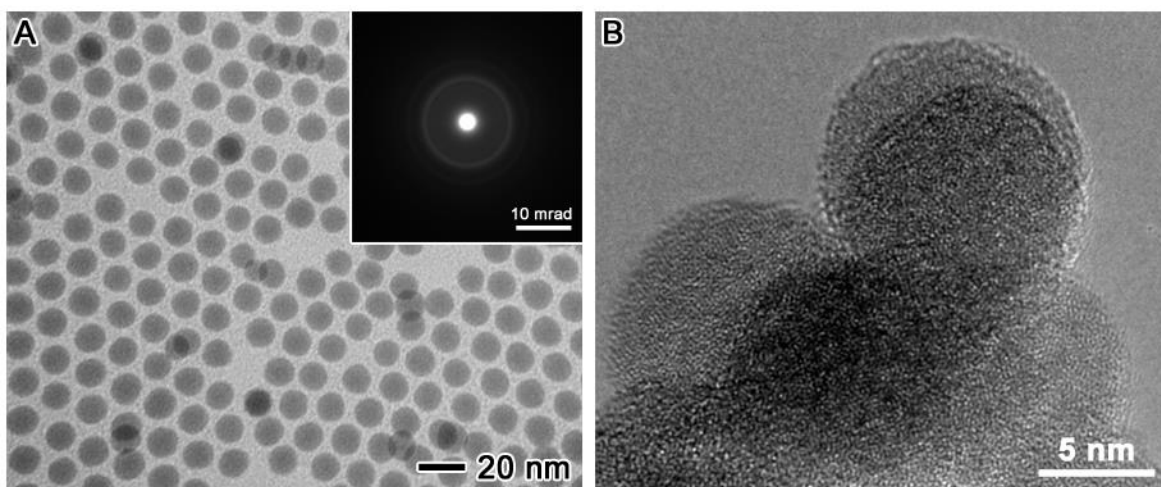


**Figure S1.** TEM characterization of NiO<sub>x</sub> nanoparticles: (A) TEM image overview with the inset of electron diffraction pattern; and (B) HRTEM image. These NiO<sub>x</sub> nanoparticles are spherical shape with an average size of 16.8 nm and have poor crystallinity.

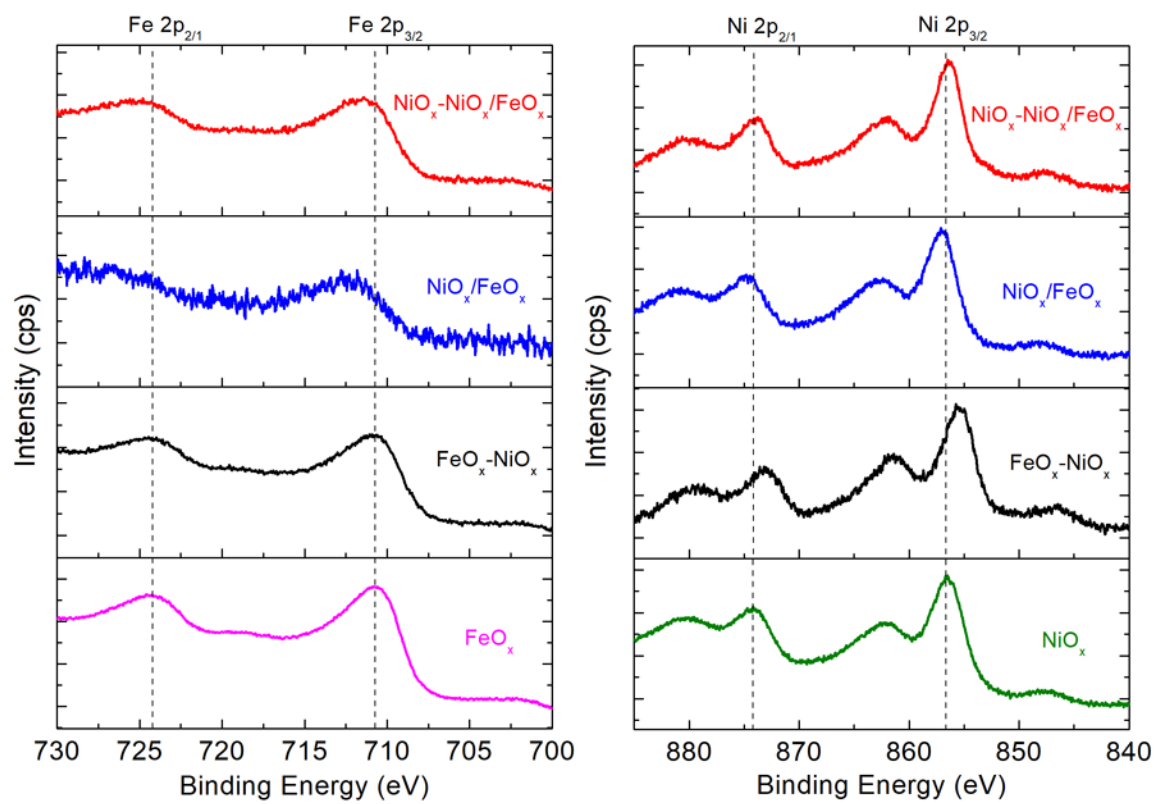


**Figure S2.** XPS spectra of Fe 2p and Ni 2p electrons for nanoparticles with different morphologies: NiO<sub>x</sub>-NiO<sub>x</sub>/FeO<sub>x</sub> core-mixed shell (red), NiO<sub>x</sub>/FeO<sub>x</sub> alloy (blue), FeO<sub>x</sub>-NiO<sub>x</sub> core-shell (black), FeO<sub>x</sub> (pink), and NiO<sub>x</sub> (green).

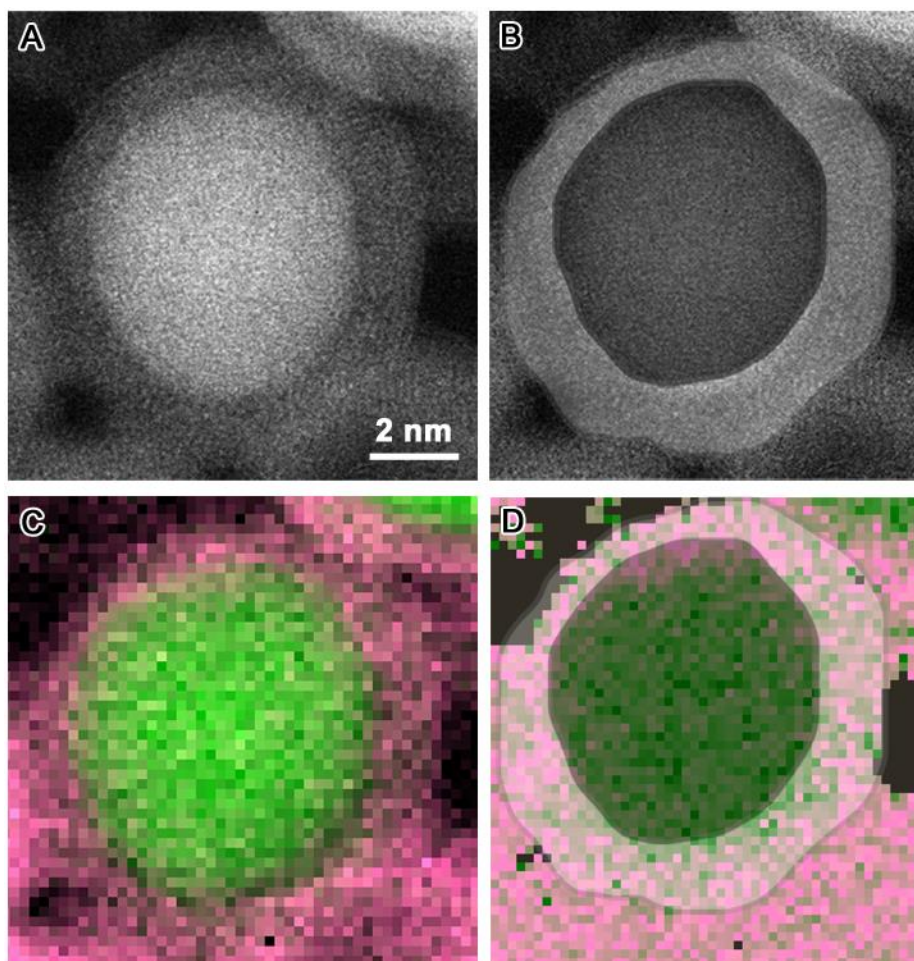


**Figure S3.** STEM images (A,B) and EELS maps (C,D) of the NiO<sub>x</sub>-NiO<sub>x</sub>/FeO<sub>x</sub> core-mixed shell structure on side-by-side panel displays. The highlighted areas in (C) and (D) illustrate the NiO<sub>x</sub>/FeO<sub>x</sub> mixed shell for elemental quantitative analysis.

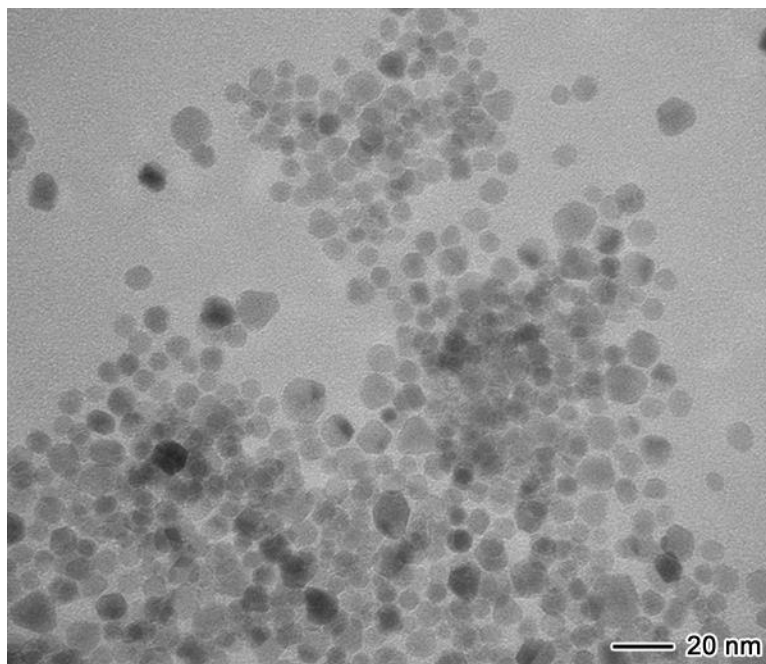


**Figure S4.** TEM image of FeO<sub>x</sub> nanoparticles.

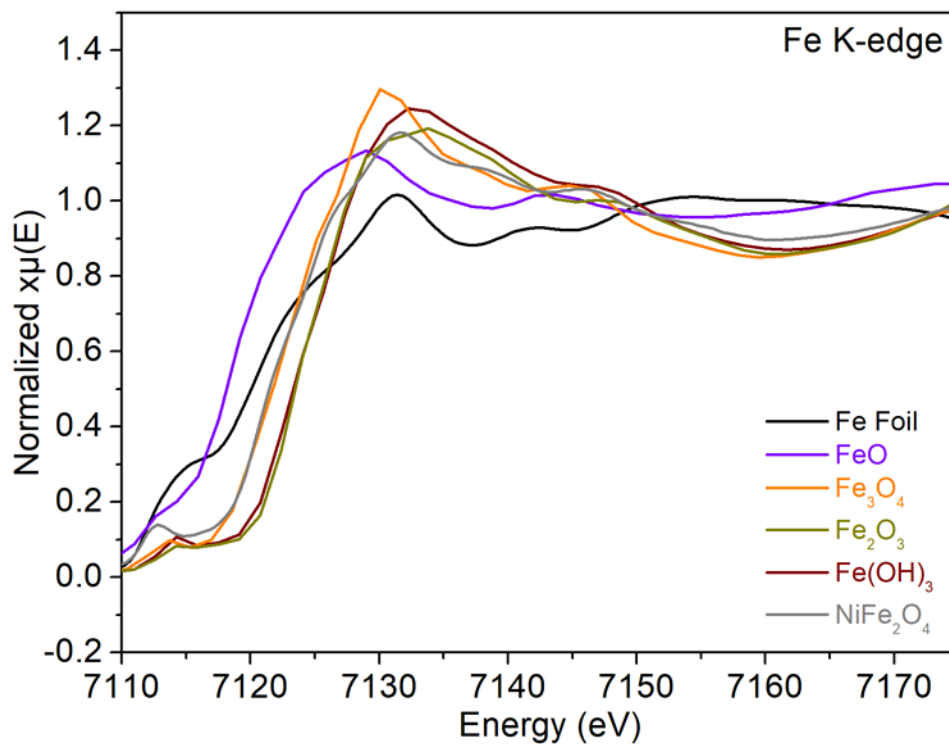


**Figure S5.** XAS spectra of Fe K-edge for Fe bulk standards: Fe foil (black), FeO (violet),  $\text{Fe}_3\text{O}_4$  (orange),  $\text{Fe}_2\text{O}_3$  (dark yellow),  $\text{Fe}(\text{OH})_3$  (wine), and  $\text{NiFe}_2\text{O}_4$  (grey).

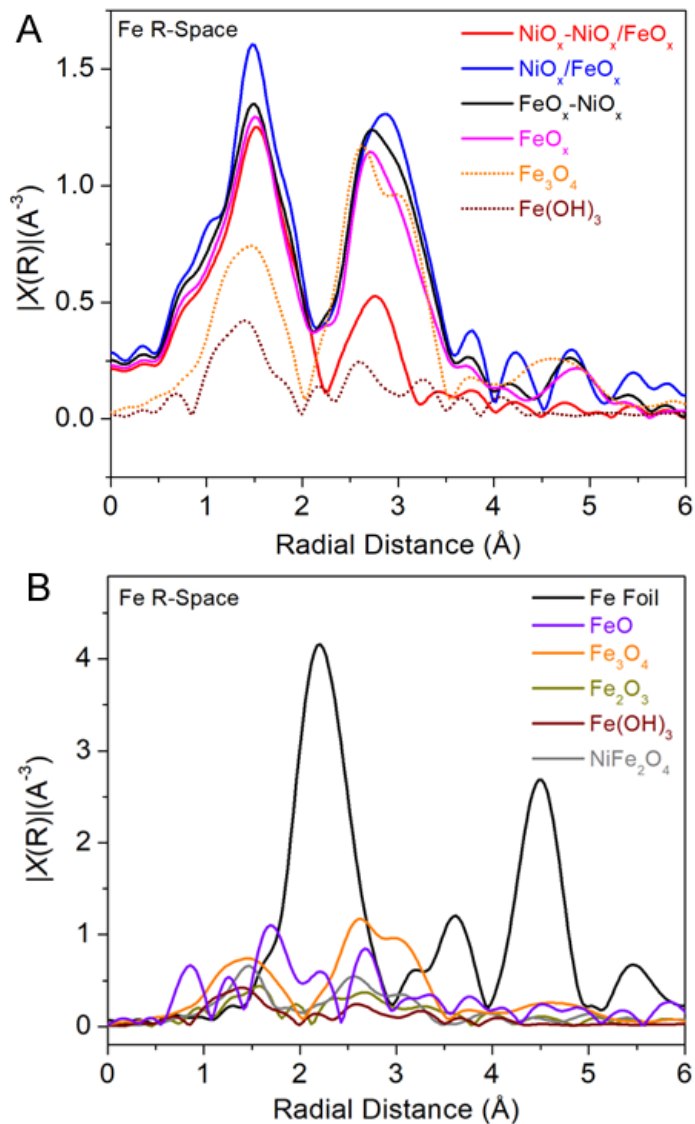


**Figure S6.** (A) EXAFS region of Fe K-edge for the nanoparticle catalysts:  $\text{NiO}_x\text{-NiO}_x/\text{FeO}_x$  core-mixed shell (red),  $\text{NiO}_x/\text{FeO}_x$  alloy (blue),  $\text{FeO}_x\text{-NiO}_x$  core-shell (black), and  $\text{FeO}_x$  (pink). The EXAFS region of selected Fe bulk standards were plotted in dash curves:  $\text{Fe}_3\text{O}_4$  (orange) and  $\text{Fe(OH)}_3$  (wine). (B) EXAFS region of Fe K-edge for Fe bulk standards: Fe foil (black),  $\text{Fe}_3\text{O}_4$  (orange),  $\text{Fe}_2\text{O}_3$  (dark yellow),  $\text{Fe(OH)}_3$  (wine), and  $\text{NiFe}_2\text{O}_4$  (grey). The plots were not corrected for the phase shift.

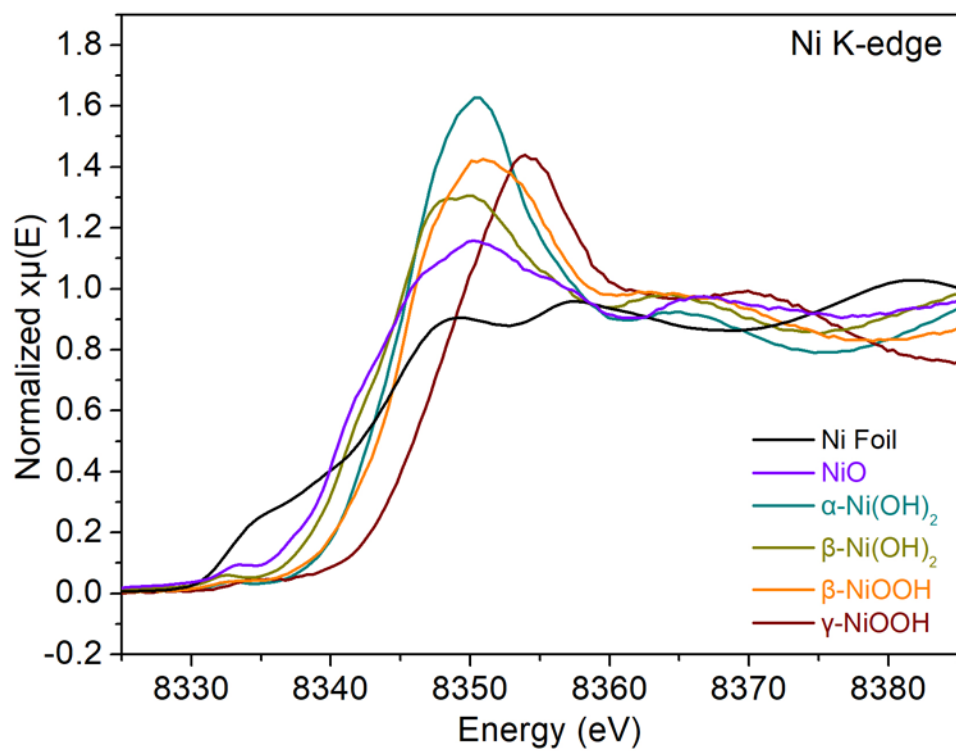


**Figure S7.** XAS spectra of Ni K-edge for Ni bulk standards: Ni foil (black), NiO (violet),  $\alpha$ -Ni(OH)<sub>2</sub> (dark green),  $\beta$ -Ni(OH)<sub>2</sub> (dark yellow),  $\beta$ -NiOOH (orange), and  $\gamma$ -NiOOH (wine).

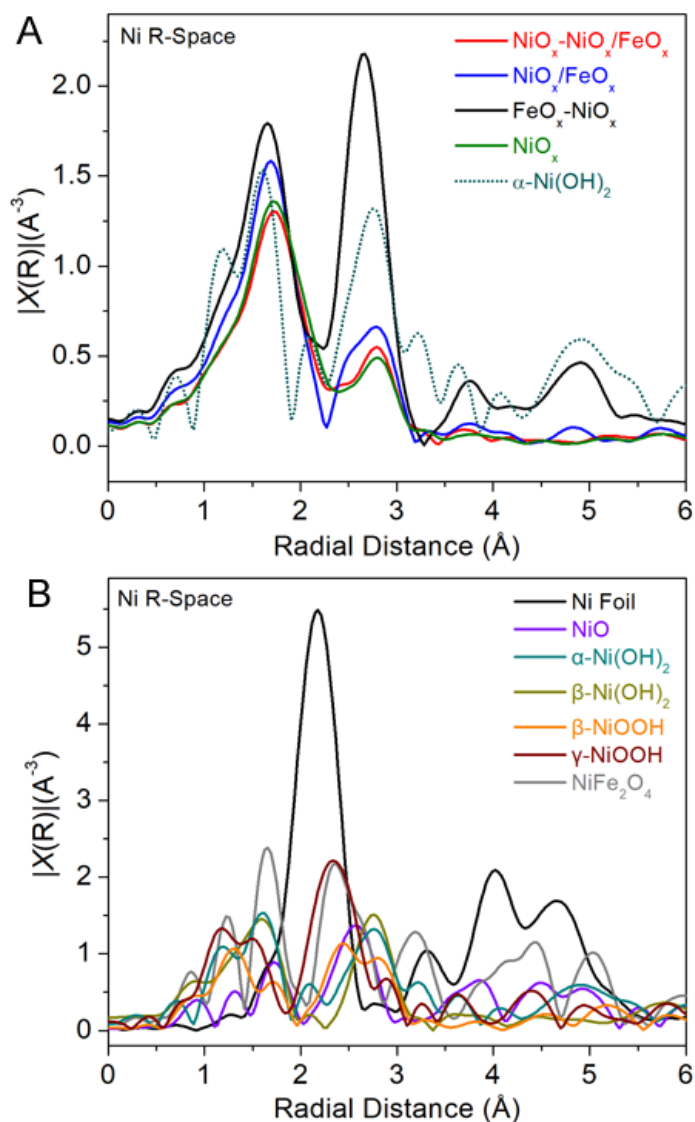


**Figure S8.** (A) EXAFS region of Ni K-edge for the nanoparticle catalysts:  $NiO_x-NiO_x/FeO_x$  core-mixed shell (red),  $NiO_x/FeO_x$  alloy (blue),  $FeO_x-NiO_x$  core-shell (black), and  $NiO_x$  (green). The EXAFS region of  $\alpha-Ni(OH)_2$  bulk standard was plotted in a dark green dash curve. (B) EXAFS region of Ni K-edge for Ni bulk standards: Ni foil (black), NiO (violet),  $\alpha-Ni(OH)_2$  (dark green),  $\beta-Ni(OH)_2$  (dark yellow),  $\beta-NiOOH$  (orange),  $\gamma-NiOOH$  (wine), and  $NiFe_2O_4$  (grey). The plots were not corrected for the phase shift.

**Table S2.** TOF values for each nanocatalyst calculated based on the Ni concentration either from the ICP-MS analysis ( $\text{TOF}_{\text{ICP-MS}}$ ) or the redox wave integration ( $\text{TOF}_{\text{redox wave}}$ ) assuming 1 or 1.5 electron transfer per Ni atom.

nanocatalysts	$\text{TOF}_{\text{ICP-MS}} (\text{s}^{-1})$	$\text{TOF}_{\text{redox wave}} (\text{s}^{-1})$ ( $m = 1$ )	$\text{TOF}_{\text{redox wave}} (\text{s}^{-1})$ ( $m = 1.5$ )
$\text{NiO}_x\text{-NiO}_x/\text{FeO}_x$	1.175	5.46	8.19
$\text{NiO}_x/\text{FeO}_x$	0.090	2.13	3.20
$\text{FeO}_x\text{-NiO}_x$	0.003	0.15	0.22
$\text{NiO}_x$	0.006	0.10	0.16

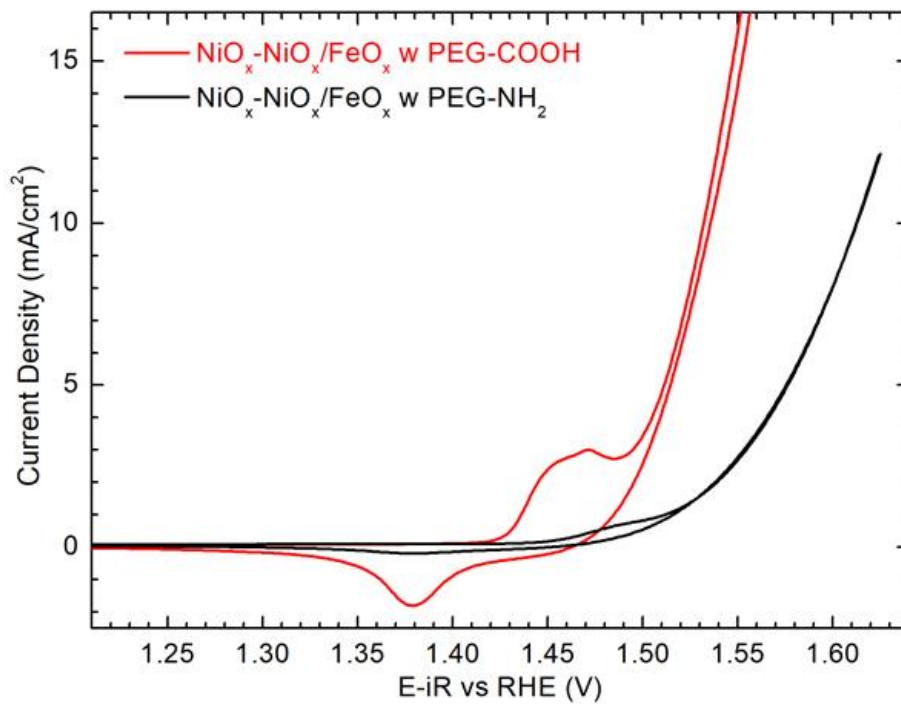


**Figure S9.** CV profiles of the nanoparticle catalysts obtained in 1 M KOH at a scan rate of 10 mV/s: NiO<sub>x</sub>-NiO<sub>x</sub>/FeO<sub>x</sub> core-mixed shell with PEG-COOH surface ligand (red) and NiO<sub>x</sub>-NiO<sub>x</sub>/FeO<sub>x</sub> core-mixed shell with PEG-NH<sub>2</sub> surface ligand (black).

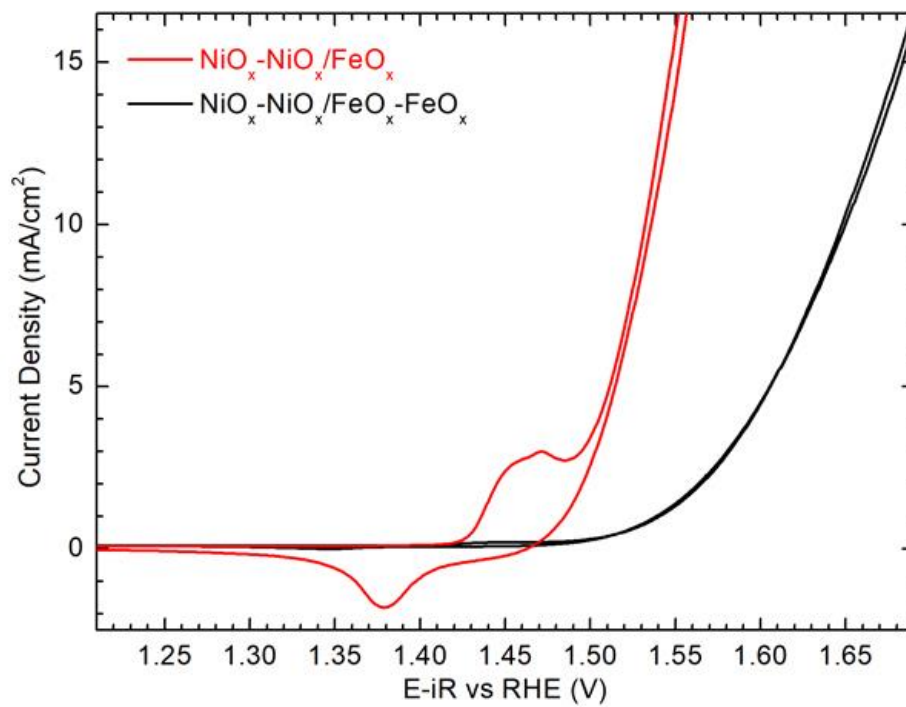


**Figure S10.** CV profiles of the nanoparticle catalysts obtained in 1 M KOH at a scan rate of 10 mV/s: NiO<sub>x</sub>-NiO<sub>x</sub>/FeO<sub>x</sub> core-mixed shell (red) and NiO<sub>x</sub>-NiO<sub>x</sub>/FeO<sub>x</sub>-FeO<sub>x</sub> core-mixed shell-shell (black).

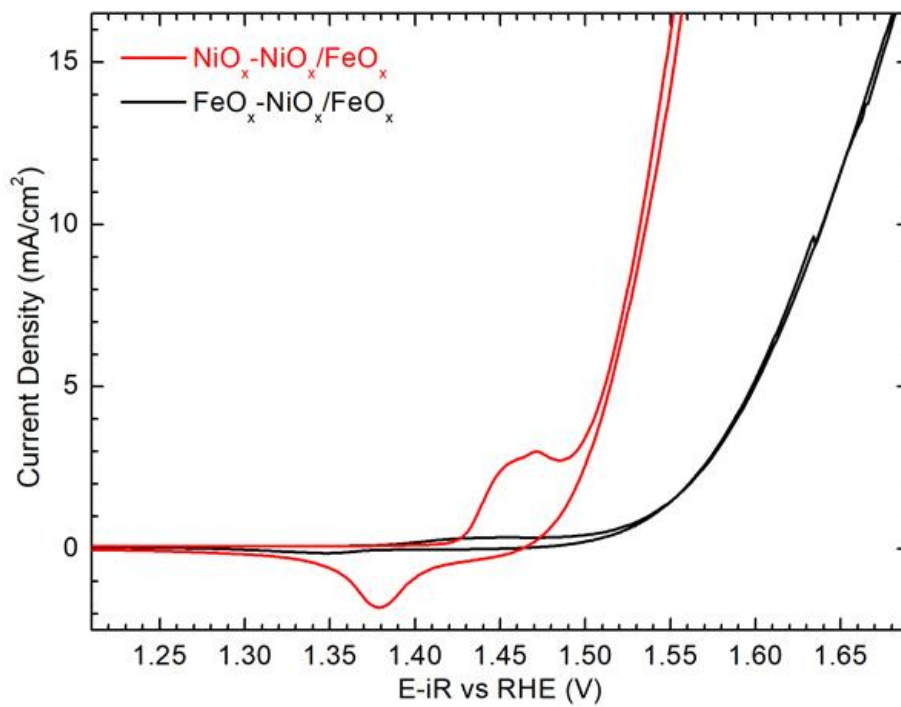


**Figure S11.** CV profiles of the nanoparticle catalysts obtained in 1 M KOH at a scan rate of 10 mV/s: NiO<sub>x</sub>-NiO<sub>x</sub>/FeO<sub>x</sub> core-mixed shell (red) and FeO<sub>x</sub>-NiO<sub>x</sub>/FeO<sub>x</sub> core-mixed shell (black).

## References:

- (1) Egerton, R. F. *Electron Energy-Loss Spectroscopy in the Electron Microscope*, 3rd ed.; Springer Science+Business Media: New York, 2011; pp 270-277.
- (2) Stevens, M. B.; Enman, L. J.; Batchellor, A. S.; Cosby, M. R.; Vise, A. E.; Trang, C. D.; Boettcher, S. W., Measurement techniques for the study of thin film heterogeneous water oxidation electrocatalysts. *Chemistry of Materials* **2016**, 29 (1), 120-140.
- (3) 10. Smith, R. D.; Berlinguette, C. P., Accounting for the dynamic oxidative behavior of nickel anodes. *Journal of the American Chemical Society* **2016**, 138 (5), 1561-1567.